

NAVAL POSTGRADUATE SCHOOL

Monterey, California



THESIS

DAMAGE PRODUCED BY THE FREE ELECTRON LASER

by

Lee R. Short

June 1999

Thesis Advisor:
Co-Advisor:

William B. Colson
Robert L. Armstead

Approved for public release; distribution is unlimited.

REPORT DOCUMENTATION PAGE			Form Approved OMB No. 0704-0188	
Public reporting burden for this collection of information is estimated to average 1 hour per response, including the time for reviewing instruction, searching existing data sources, gathering and maintaining the data needed, and completing and reviewing the collection of information. Send comments regarding this burden estimate or any other aspect of this collection of information, including suggestions for reducing this burden, to Washington headquarters Services, Directorate for Information Operations and Reports, 1215 Jefferson Davis Highway, Suite 1204, Arlington, VA 22202-4302, and to the Office of Management and Budget, Paperwork Reduction Project (0704-0188) Washington DC 20503.				
1. AGENCY USE ONLY (Leave blank)		2. REPORT DATE June 1999		3. REPORT TYPE AND DATES COVERED Master's Thesis
4. TITLE AND SUBTITLE DAMAGE PRODUCED BY THE FREE ELECTRON LASER				5. FUNDING NUMBERS
6. AUTHOR(S) Short, Lee R.				
7. PERFORMING ORGANIZATION NAME(S) AND ADDRESS(ES) Naval Postgraduate School Monterey, CA 93943-5000				8. PERFORMING ORGANIZATION REPORT NUMBER
9. SPONSORING / MONITORING AGENCY NAME(S) AND ADDRESS(ES)				10. SPONSORING / MONITORING AGENCY REPORT NUMBER
11. SUPPLEMENTARY NOTES The views expressed in this thesis are those of the author and do not reflect the official policy or position of the Department of Defense or the U.S. Government.				
12a. DISTRIBUTION / AVAILABILITY STATEMENT Approved for public release; distribution is unlimited.				12b. DISTRIBUTION CODE
13. ABSTRACT (maximum 200 words) The first damage experiments produced by a Free Electron Laser were conducted at the Department of Energy's Thomas Jefferson National Accelerator Facility (TJNAF). In the past, only large-scale laser experiments were thought to properly model lasers for weapons applications. Scaled down procedures developed in this thesis allowed the FEL, with a few hundred watts of power, to characterize the damage produced by a megawatt weapon's scale laser. With a power density of 10 kW/cm ² , the TJNAF FEL bombards targets with a steady stream of tens of millions of pulses per second. Each pulse contains 50 MW of power in short bursts lasting 4 x 10 ⁻¹⁴ seconds each. No previous laser experiments have been conducted to explore the effects of the FEL short pulses. Target materials were obtained from the Naval Surface Warfare Center (NSWC), Port Hueneme. Data were collected and analyzed using video cameras and optical microscopes, and irradiated at TJNAF. This thesis was a productive cooperation between NPS, TJNAF, and NSWC Port Hueneme, to the benefit of DOD.				
14. SUBJECT TERMS Free Electron Laser, Directed Energy Weapons, Ship Defense				15. NUMBER OF PAGES 69
				16. PRICE CODE
17. SECURITY CLASSIFICATION OF REPORT Unclassified	18. SECURITY CLASSIFICATION OF THIS PAGE Unclassified	19. SECURITY CLASSIFICATION OF ABSTRACT Unclassified	20. LIMITATION OF ABSTRACT UL	

Approved for public release; distribution is unlimited.

DAMAGE PRODUCED BY THE FREE ELECTRON LASER

Lee R. Short
Lieutenant, United States Navy
B.S., United States Naval Academy, 1992

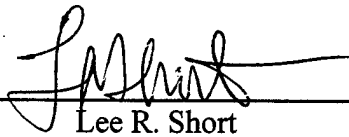
Submitted in partial fulfillment of the
requirements for the degree of

MASTER OF SCIENCE IN APPLIED PHYSICS

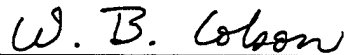
from the

**NAVAL POSTGRADUATE SCHOOL
June 1999**

Author:


Lee R. Short

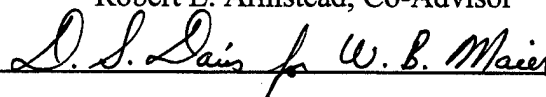
Approved by:



William B. Colson, Thesis Advisor



Robert L. Armstead, Co-Advisor



William B. Maier II, Chairman
Department of Physics

ABSTRACT

The first damage experiments produced by a Free Electron Laser were conducted at the Department of Energy's Thomas Jefferson National Accelerator Facility (TJNAF). In the past, only large-scale laser experiments were thought to properly model lasers for weapons applications. Scaled down procedures developed in this thesis allowed the FEL, with a few hundred watts of power, to characterize the damage produced by a megawatt weapon's scale laser. With a power density of 10 kW/cm^2 , the TJNAF FEL bombards targets with a steady stream of tens of millions of pulses per second. Each pulse contains 50 MW of power in short bursts lasting 4×10^{-14} seconds each. No previous laser experiments have been conducted to explore the effects of the FEL short pulses. Target materials were obtained from the Naval Surface Warfare Center (NSWC), Port Hueneme. Data were collected and analyzed using video cameras and optical microscopes, and irradiated at TJNAF. This thesis was a productive cooperation between NPS, TJNAF, and NSWC Port Hueneme, to the benefit of DOD.

TABLE OF CONTENTS

I. INTRODUCTION/BACKGROUND.....	1
A. SCENARIO OF LAYERED DEFENSE	1
B. SHORT RANGE DEFENSE (CIWS).....	5
C. MEDIUM RANGE DEFENSE (GUNS)	9
D. LONG RANGE DEFENSE (MISSILES).....	9
II. LASERS	11
A. BACKGROUND	11
B. ATMOSPHERIC PROPAGATION	13
III. FEL THEORY	21
A. BASIC OPERATION	21
B. PENDULUM EQUATION	23
C. WAVE EQUATION	27
IV. LASER MATERIAL INTERACTION	31
A. BACKGROUND	31
B. THERMAL DIFFUSION LENGTH.....	31
C. SCALING.....	34
V. LASER DAMAGE TO MATERIAL	35
A. BACKGROUND	35
B. THOMAS JEFFERSON NATIONAL ACCELERATOR FACILITY	35
C. USER LAB.....	37
D. EXPERIMENTAL PROCEDURES	39
E. PHENOLIC RESIN EXPERIMENTS	40
1. Phenolic Sample 1	40
2. Phenolic Sample 2.....	43
F. PYROCERAM EXPERIMENTS.....	47
1. Pyroceram Sample 1.....	47
2. Pyroceram Sample 2	50
VI. CONCLUSION.....	55
LIST OF REFERENCES	57
INITIAL DISTRIBUTION LIST	59

ACKNOWLEDGMENT

First and foremost, I would like to particularly thank the readers of this thesis; Bill Colson for his guidance and patience in the writing of this thesis, and Bob Armstead, for his "million dollar" advice. A thanks also goes to my friend, Breckenridge Morgan, Sr., for his computer technical support and assistance in answering my "stupid computer" questions. I cannot forget to thank Robert Thomson for his help in the writing of this thesis.

A special thanks to the personnel at TJNAF for their technical expertise and for conducting the experiments. Thanks to Michelle Shinn especially, for always being available to answer questions.

Saving the best for last, I would like to thank my wife, Holly, who gave birth to our first child, Alison, during our brief stay in Monterey. You have put your career on hold for me and our daughter. Thank you for supporting me and allowing me the time to do the work required for this thesis and master's degree. I love you.

I. INTRODUCTION/BACKGROUND

A. SCENARIO OF LAYERED DEFENSE

Consider the following scenario. You are on a U.S. Ticonderoga Class cruiser operating in the Persian Gulf in a hostile environment. An enemy aircraft at 150 nautical miles from your ship has just launched a Russian-bought Anti-Ship Missile (ASM) at you. It travels at Mach 3 (3 nautical miles (nm) every 6 seconds). From a range of 150 nm, the ASM will impact your ship in 300 seconds. However, since it is a sea-skimming missile that flies at 8 meters off the water, you will not be able to see it until it comes over the horizon. Your horizon range is 11 nm, based on a Phalanx Close-In-Weapons-System (CIWS) height of 25 meters. This gives you 22 seconds from the point you can see the ASM until it impacts your ship. This is not a lot of reaction time to detect, track, and decide to shoot the ASM down.

Since your ship is a state-of-the-art Aegis cruiser, you have the Cooperative Engagement Capability (CEC). CEC allows other ships in your battle group to track the inbound ASM and provide targeting data for you to shoot it down while it is over the horizon. Assume it takes 40 seconds to detect, track, and react to the incoming ASM. The ASM is now at a range of 130 nm and will impact your ship in 260 seconds. Still further, your anti-ASM missiles, traveling at Mach 1.5, need to travel some distance to intercept the inbound ASM, decreasing the time and range you have to safely destroy the ASM before it impacts your ship. You launch two anti-ASM missiles to intercept the ASM at 260 seconds to impact. In a perfect scenario, your anti-ASM missiles are on

target. At a closure rate of Mach 4.5 (4.5 nm every 6 seconds), one or both of them intercepts the ASM 173 seconds later and splashes it at a range of 43 nm.

In a Navy training exercise I participated in, 2 out of 16 standard missiles hit inbound targets in an easier line of sight scenario. In a harder over the horizon scenario, the odds of hitting a sea-skimming inbound ASM would be significantly decreased. So, what if your anti-ASM missiles miss? You now have 87 seconds to try another missile or switch to guns.

You switch to guns. Your guns have a maximum range of 13 nm with shell speeds of Mach 1. You are worried because the missile is currently out of the maximum range of your guns. You calculate and shoot the gun rounds to intercept the ASM at their maximum range of 13 nm. The current gun systems have no capability to track and shoot down a target at such high speeds. At 13 nm, the shells could be dispersed as far as 100 meters off target. The guns accuracy will be nominal because you are shooting at a target over the horizon. Say, you are very lucky and a gun round intercepts the ASM at 13 nm and splashes it. Great shot!

Again, the odds are against you. The chances of hitting an inbound ASM at Mach 3 are slim to none. At a range of 13 nm, you now have 26 seconds until the ASM hits your ship. You switch to the last layer of defense, the Phalanx Close-In-Weapons-System (CIWS). Unfortunately, the CIWS has a maximum detection range of 2.5 nm and an effective range of 1 nm. At that range, even if you hit the ASM with a CIWS shell, the shrapnel is still travelling at Mach 3 and will hit the ship anyway. At that speed, even small pieces of shrapnel will have enough momentum to cause severe damage to your ship.

The preceding scenario could happen anywhere in the world, not just the Persian Gulf. With the recent fall of the Soviet Union and their sluggish economy, their stockpile of state of the art weapons is finding it's way into the hands of countries willing to pay the price for them. The foreign policy of the United States has put its armed forces into harms way numerous times. The world political arena has mandated the U.S. Navy to transition from open ocean confrontations to littoral warfare. Being so close to shore, the need for increased ship self-defense is needed now more than ever.

The U.S. needs to improve its ASM defense capabilities. Doctrine has evolved to increase detection, tracking, and reaction times in order to allow more time for a ship to engage inbound ASMs at further ranges. However, at closure speeds of up to Mach 3, time is of the essence. The United States' self-defense weapons are state-of-the-art, but cannot safely and quickly destroy ASMs due to the high closure rates encountered.

A new weapon to combat ASMs is being developed that uses the speed of light: the laser. Compared to current weapons, the laser takes the time to intercept out of the equation because laser light travels at 3×10^5 kilometers per second. Compared to the speed of light, the ranges are nominal and the ASMs could be destroyed in milliseconds.

Let's go back to the scenario above. Theoretically, the range of a laser is infinite. Atmospheric conditions decrease the range of a laser to less than 20 nm. Therefore, you are confined to detecting and tracking the ASM to when it pops up over the horizon at 11 nm. However, as soon as the ship can see the ASM it can be destroyed in milliseconds using a ship self-defense laser. In this sense, the ship self defense laser should be considered to replace the CIWS.

Military research programs have developed and tested lasers since the 1970s. In the 1980's, President Reagan initiated the Strategic Defense Initiative to study the feasibility of space-based lasers for ballistic missile defense. The current Air Force Airborne Laser (ABL) program has shown that the destruction of targets is feasible. The ABL is an air based chemical laser that uses dangerous chemicals that produce dangerous byproducts. A chemical laser would not be complementary to the close quarters found on a ship. Also, every shot of the ABL depletes its chemical source. For these reasons, the ABL may be impractical for ship self-defense.

The Free Electron Laser (FEL) is being studied for ship self-defense applications at Thomas Jefferson National Accelerator Facility (TJNAF) and other facilities throughout the United States. The FEL has several advantages over conventional lasers that make it optimal for ship self-defense. The FEL is powered by the ship's electrical system, not chemicals. The FEL is also tunable to various frequencies allowing it to overcome various hurdles such as atmospheric attenuation.

This thesis concentrates on laser ablation experiments on various missile materials conducted at TJNAF. Various samples of missile nosecones were ablated by the TJNAF FEL at various power settings. The test shots were observed and studied to research the effects of the FEL on the various materials. The research is vital to determine the viability of a ship-based laser.

B. SHORT RANGE DEFENSE (CIWS)

The Phalanx-Close-In-Weapons System (CIWS) was designed from the bottom up to be the last layer of defense for a ship. It is a stand-alone system consisting of a self-supported fire control and tracking radar and a 20-mm Gatling gun. Its maximum detection range is 2.5 nm with a maximum effective range of 1 nm. The 20-mm Gatling gun fires depleted uranium penetrators. It has a firing rate of 4500 rounds per minute (rds/min), though it typically fires several hundred rounds in bursts. On an Aegis Cruiser, the CIWS is mounted at 25 meters above the sea. An ASM flying at 8 meters above the sea will have a horizon distance of about 11 nm.

The CIWS has several deficiencies. Due to the high firing rate, it can overheat easily after sustained use. The high firing rate also causes heavy vibration in the Gatling gun. Vibrations that shake the barrel tip up and down by just a few milliradians can cause the penetrators to stray off target at long ranges. The CIWS has a limited shell magazine. At 4500 rds/min, even short bursts of several hundred rounds will quickly deplete the magazine, allowing for limited engagements.

A computer simulation was constructed to describe the performance of the CIWS against an inbound ASM. Figure (I.B.1) shows CIWS's probability of hitting a missile versus its range from ship. The odds of hitting the missile get better as it gets closer. The plot shows that at a range of 250 meters, your chances of hitting the missile are about 50%. The good news is there is a good chance you will hit the missile with a penetrator. The bad news is you don't actually hit it until it's almost too late. At ranges closer than 250 meters, the missile fragments can still impact your ship and cause serious damage.

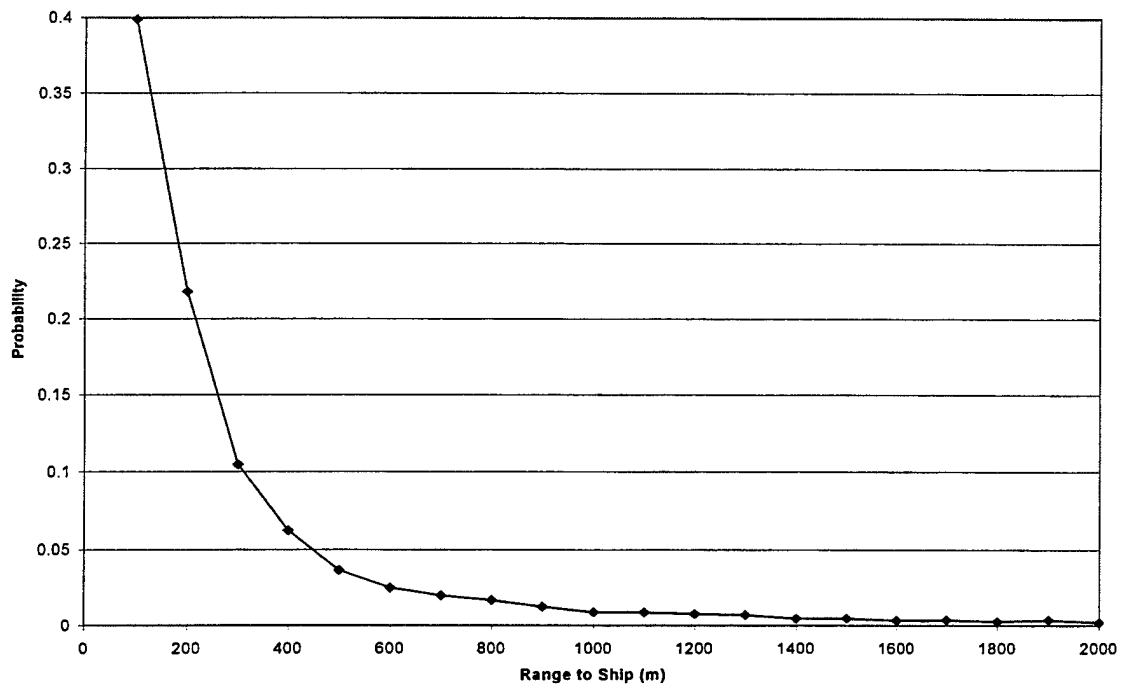


Figure I.B.1. CIWS's probability of hitting a missile versus its range from ship.

In Fig. (I.B.2), the effectiveness of CIWS is clarified. The number of accumulated hits versus range is plotted for the CIWS with a dispersion of 0.002, a firing rate of 4500 rds/min and incoming missile speed of Mach 1. Figure (I.B.2) shows that the ASM will be killed at a range of approximately 450 meters from the ship assuming it takes 8 penetrators impacting the missile to destroy it.

Further computer simulations illustrated the trajectories of the missile fragments after penetrators destroyed the missile. The typical missile kill range was determined to be 100-200 meters from the ship [Ref. 1]. We assume the missile was killed at 200 meters. Upon exploding, it generates fragments of varied sizes, shapes and velocities.

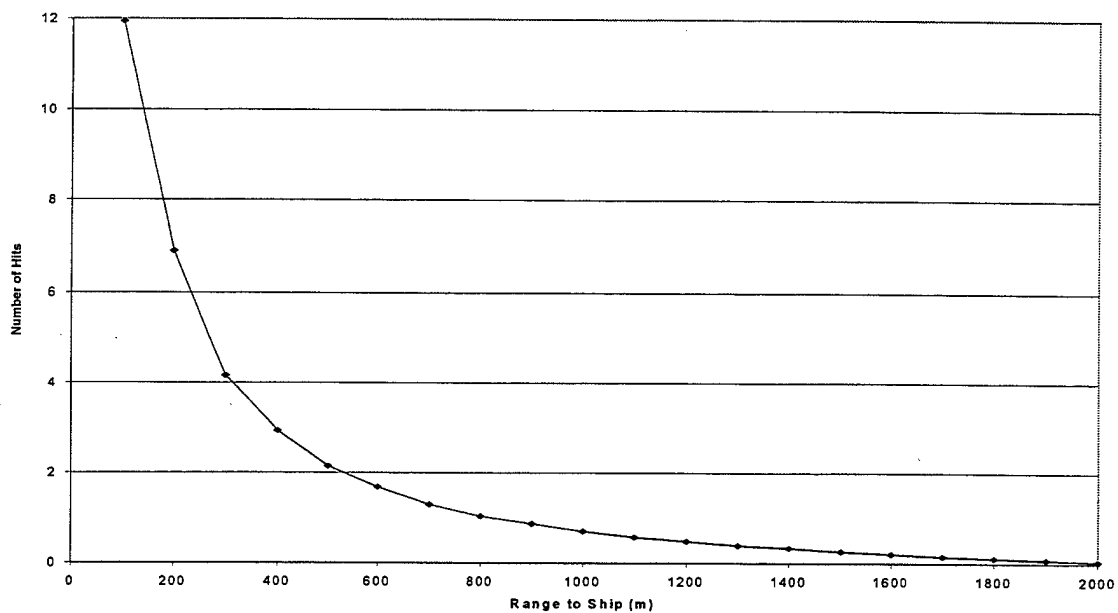


Figure I.B.2. Number of accumulated hits versus range.

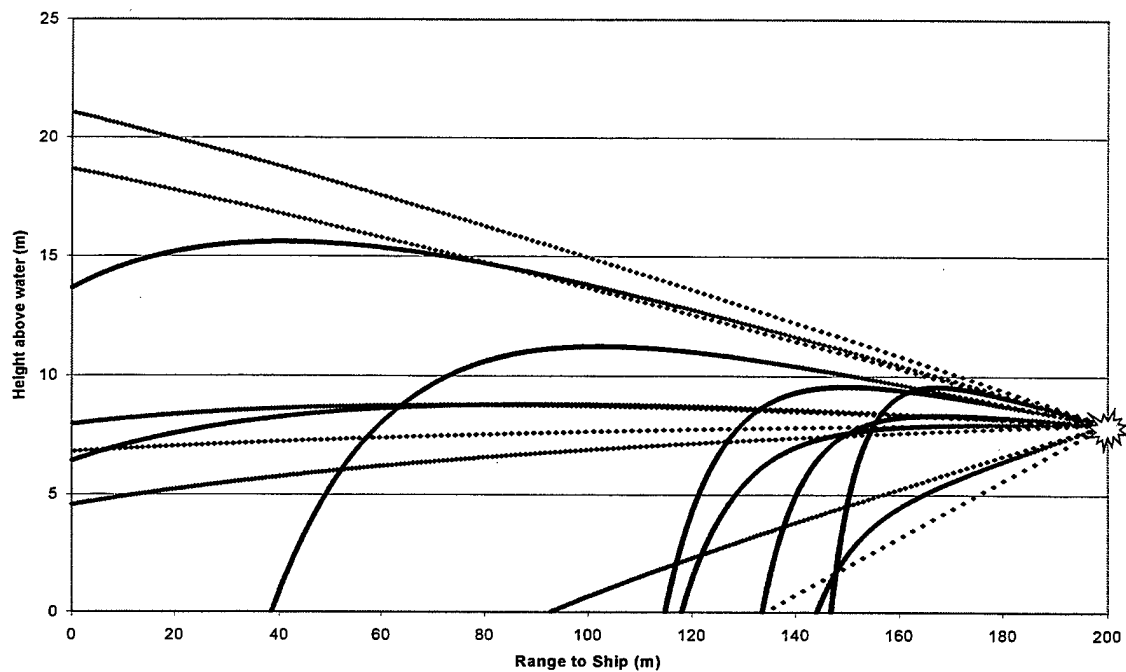


Figure I.B.3. Ballistic trajectories of the largest 15 inbound fragments of various sizes and shapes.

Figure (I.B.4) shows the probability of a missile fragment hitting the ship versus missile destruction range. The probability a fragment will hit the ship at a range of probable kill means that a defense weapon needs a faster response time.

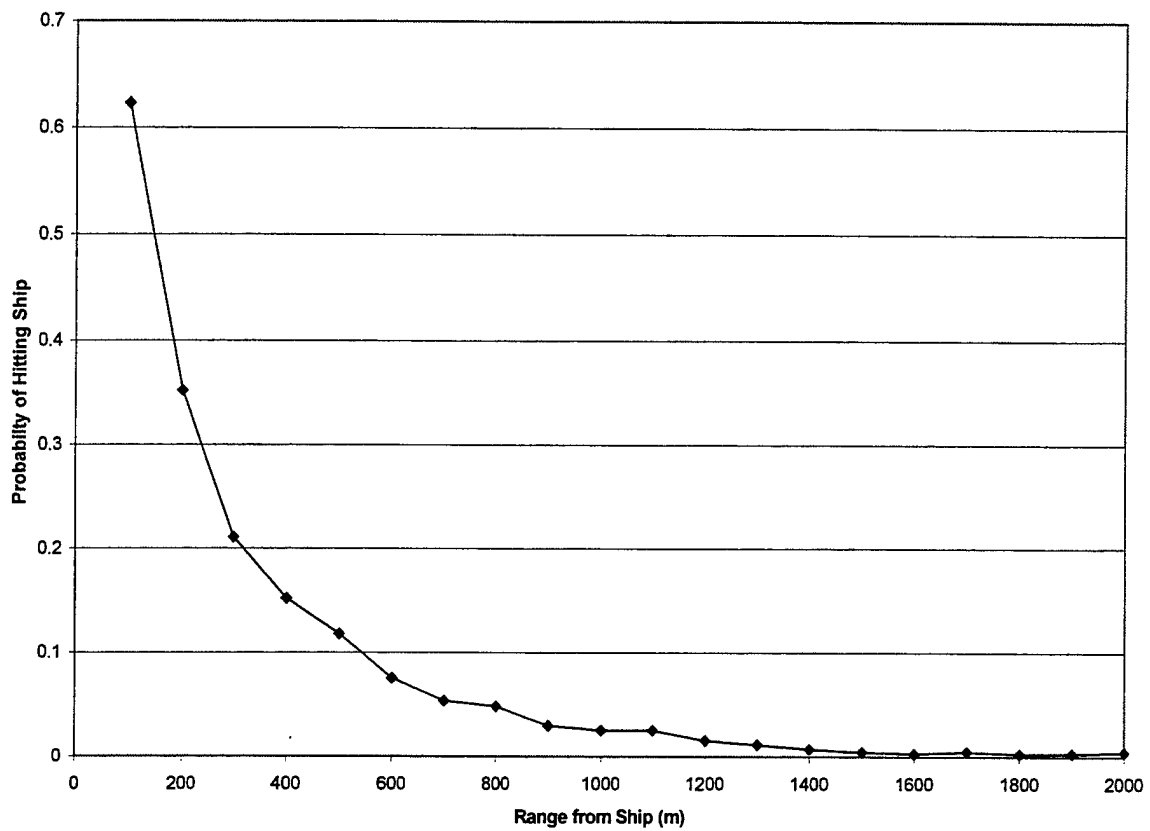


Figure I.B.4. Probability of a missile fragment hitting the ship versus missile destruction range.

C. MEDIUM RANGE DEFENSE (GUNS)

The standard navy gun is the 5 inch, 54 caliber gun. It has a maximum range of 13 nm. Its maximum effective range is lower, about 9 nm. The gun shells leave the barrel with a muzzle velocity above Mach 1. Due to friction and drag, however, the shells slow to subsonic speeds as they travel to the target. Its primary mission is to provide fire support but it can be used for self-defense.

Current gun fire control systems for gun systems have no capability to track and shoot down a target at such high speeds. Current Aegis fire control systems will not engage inbound targets at speeds above Mach 1. Firing shells out to a range of 13 nm would make accuracy minimal. The shells could be dispersed as far as 100 meters off target. Also, the speed of the shell travelling to the target is subsonic causing a delay in response time. The response time directly correlates to the proximity of kill. A defense weapon with a faster response time is required.

D. LONG RANGE DEFENSE (MISSILES)

For years, the U.S. Navy has relied on the Standard Missile (SM-1 and SM-2) for surface to air engagements. Their primary mission is to engage and destroy inbound aircraft flying at high altitudes. Destroying ASMs is not one of their primary roles, though they can be used in this capacity as described in the previous scenario. The sea-skimming aspect of the ASM does not allow for a high probability destruction of the ASM. In essence, the best odds a standard missile has against an inbound ASM is when the ASM is still in the vicinity of the firing aircraft. In a perfect world, the standard missile destroys the inbound aircraft before it even launches the ASM.

Through the years, research and development has increased the range of the standard missile. The SM-1's range was initially 30 nm and increased to 60 nm with the addition of a booster. The earlier version of the SM-2 had a range of 60 nm and was increased to 90 nm with a booster addition. Current SM-2s have a range of over 100 nm with speeds above Mach 3.

The most advanced Aegis Cruisers fire standard missiles via the vertical launch systems. After firing, a standard missile flies to an altitude of 30 kft, then tips over to search for its target. This flight profile delays the destruction of an inbound ASM by seconds. Future standard missiles are being researched and developed to have a more adequate flight profile specifically to combat inbound ASMs.

The range of the standard missile does not hinder its capability to shoot down an ASM. The sea-skimming capability of current ASMs is the hindrance. Assuming the ASM flies at 8 meters above the sea and our detection and tracking radars are mounted at 25 meters above the sea, our horizon distance is approximately 11 nm. At closure speeds of Mach 4.5 and higher, the ASM would still be destroyed at an approximate range of 3 nm from the ship. In this sense, the standard missile is a good weapon to use against an inbound ASM. However, the range of destruction is still dependent on everything happening in a perfect timeline. The harsh reality of such a close kill is that the Navy requires a self-defense weapon with a faster response time.

II. LASERS

A. BACKGROUND

In the previous section, we showed that CIWS and guns are virtually ineffective against current ASMs. Anti-ASM missiles are being developed and improved in order to keep up with the increasing technology of current ASMs. Although these weapons are state-of-the-art, they share a common disadvantage: their reaction time is slow compared to the speeds of current ASMs. In this thesis, I suggest that directed energy weapons (DEW), specifically the Free Electron Laser (FEL), be investigated for future anti-ASM use.

Is the laser weapon a fantasy or is it viable? When you think of lasers, you think of weapons used in fantasy movies, such as Star Wars or Star Trek. In the 1980's, the Navy's Mid-Infrared Advanced Chemical Laser (MIRACL) "successfully engaged BQM-34s and supersonic Talos/Vandal missiles in crossing scenarios at tactically meaningful ranges" [Ref. 2]. The MIRACL laser program determined that a power density of approximately 10 kW per square centimeter on target was required for a kill. Recently, the USA Today reported that "Lasers will change the face of warfare" when it published an article describing the Air Force's Airborne Laser (ABL) [Ref. 3]. Lasers are a fantasy idea that have been realized in the real world.

Research and development (R&D) has shown us the advantages and disadvantages of lasers. A laser is nothing more than a blowtorch that reaches out to the target at the speed of light [Ref. 4]. In a perfect world, if a target is in view, the laser should be able to kill it. R&D also showed that lasers can experience power losses on

target due to atmospheric attenuation and thermal blooming. These extinction factors take energy away from the laser intensity at the target diminishing the beam's capacity for a kill.

Chemical lasers don't perform adequately as a ship self-defense weapon. The Air Force's ABL and the Navy's MIRACL are chemical lasers. They use dangerous chemicals that produce dangerous chemical by-products and are incompatible with a ship's close quarters. Also, they have fixed wavelengths. Their wavelengths were chosen as carefully as possible to exploit a specific atmospheric propagation window but proved to be inadequate because of thermal blooming on account of the variability of the windows with atmospheric conditions [Ref. 5].

The FEL is the better choice for a ship self-defense laser. The FEL is powered by the ship's own electrical system. A modified shipboard distribution system placed onboard a ship could provide an unlimited magazine [Ref. 6]. Atmospheric absorption could be largely overcome due to the tunability of the FEL. The FEL would allow for the selection of laser beams with varied wavelengths to exploit the variable "windows" of maximum transmission. With a more precise selection of wavelength, the FEL could avoid thermal blooming. On March 11, 1999, Thomas Jefferson National Accelerator Facility (TJNAF) lased at 710 W. This amount of power does not come close to the power required to kill an ASM defined by Albertine and Cook. With upgrades, TJNAF has plans to raise the power to 20 kW by fiscal year 2001 [Ref. 7].

B. ATMOSPHERIC PROPAGATION

The purpose of this section is to describe how a laser propagates through the atmosphere. As the laser propagates through air, the beam energy may heat up the air depending on the absorption at the wavelength used. The air dissipates the laser beam's energy like resistance in an electrical circuit dissipates energy, producing heat. The heating up of air causes thermal blooming, which is a defocusing of the beam by a change of the refractive index where the air is heated. Since we require as much intensity on the target as possible to destroy it, thermal blooming is a property we need to understand and study in order to minimize it.

We must first need to understand what it takes to kill a target, i.e. how much energy needs to be deposited on target for a kill. Energy flux, Φ , is the power density of the laser beam and is defined as the ratio of the beam's power, P , to the laser beam spot size, A ,

$$\Phi = \frac{P}{A}. \quad (\text{II.B.1})$$

In the far field, the laser beam area is $A = \pi(R\theta)^2$, where R is the range and θ is the beam half angle. Thus, Eq. (II.B.1) becomes

$$\Phi = \frac{P}{\pi(R\theta)^2}. \quad (\text{II.B.2})$$

Energy fluence, F , is the amount of energy deposited on a target in a given time.

Therefore, integrating Φ with respect to time, t , gives us

$$F = \int_0^{\tau} \Phi dt = \Phi \tau, \quad (\text{II.B.3})$$

where τ is the beam pulse duration and we have assumed a constant Φ . For a diffraction-limited beam, $\theta = 1.22\lambda/D$, where D is the diameter of the beam aperture and λ , the wavelength of the beam. Substitution of this into Φ , from Eq. (II.B.1), gives us,

$$\Phi = 0.21 \frac{PD^2}{(\lambda R)^2}, \quad (\text{II.B.4})$$

resulting in a fluence of

$$F = 0.21 \frac{PD^2 \tau}{(\lambda R)^2}. \quad (\text{II.B.5})$$

Fluence is the measure of how much energy is incident on the target. If the target has a high resistance to fluence (a high fluence threshold), it is harder for the laser to do damage. This derivation is based on the assumption that the beam is travelling through a vacuum.

A laser beam used for ship defense travels through the atmosphere. The atmosphere can cause attenuation depending on its wavelength. Transmittance is the ratio of initial beam energy to the transmitted beam energy allowed to pass through the medium. Figure (II.B.1) shows atmospheric transmittance values for wavelengths ranging 0-15 micrometers (μm), over a 1820-meter horizontal path at sea level [Ref. 8]. You can see in the figure that the selection of wavelength is important because it directly relates to how much transmittance the atmosphere allows. Figure (II.B.1) shows a transmittance value of 0-90% depending on wavelength affecting the fluence calculated in Eq. (II.B.5).

The two main mechanisms associated with propagation through the atmosphere are scattering and absorption. As the laser beam's incident energy collides with particles

in the atmosphere, the energy can be either scattered or absorbed. Scattering can be defined as the re-direction of energy due to collisions with particles, such as water vapor, that are present in the atmosphere. Absorption occurs when the incident energy is absorbed in the air. Too much scattering or absorption will diminish the beam energy reducing the damage on target.

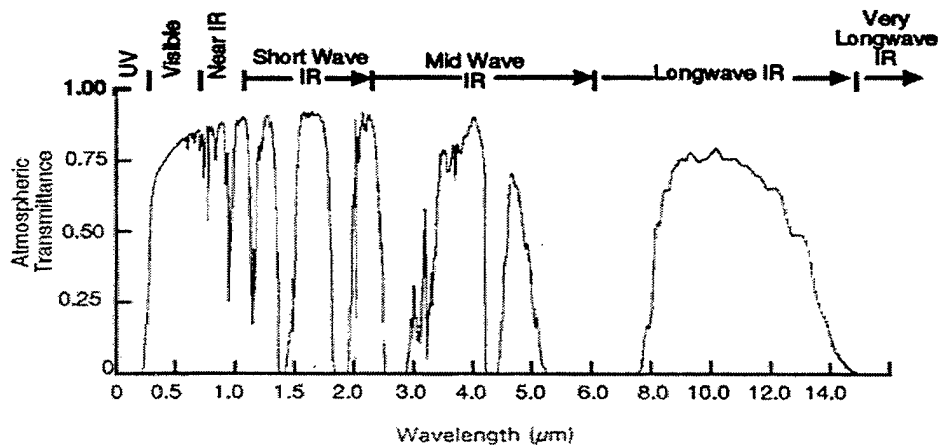


Figure II.B.1. Atmospheric transmittance for 0-15 μm . From Ref [8].

Figure (II.B.2) separates the two factors that cause attenuation for a wavelength range of 0.1-100 μm [Ref. 9]. It is a maritime aerosol model indicative of an atmosphere that a ship-based defense laser might encounter. It shows the contributions of the representative scattering and absorption coefficients to the extinction coefficient, which can be related to transmittance. Figures (II.B.1) and (II.B.2) must be taken into consideration when choosing the wavelength at which our ship self-defense laser will operate.

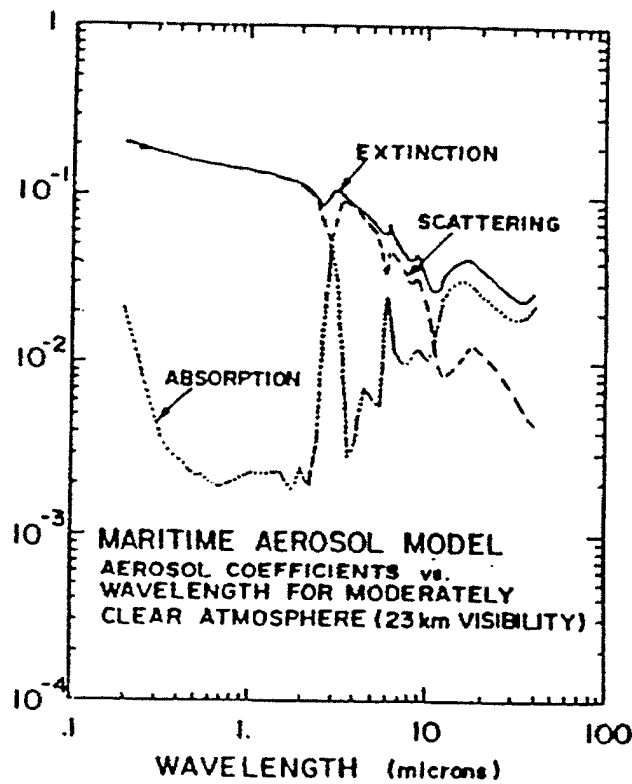


Figure II.B.2. Maritime aerosol attenuation coefficients. From Ref [8].

Inspection of Fig. (II.B.2) shows that the extinction coefficient is predominantly made up of the scattering coefficient for lower wavelengths up to 10 μm . Above 10 μm , the absorption coefficient dominates the extinction coefficient, which exacerbates thermal blooming at long wavelengths. Thermal blooming is caused by a change in the index of refraction due to the heating of air.

Figure (II.B.3) is a simulation model showing how thermal blooming effects the laser beam. Note that the energy that is dispersed detracts from the energy we can put on target. Thermal blooming is non-linear in nature and increasing power to the beam doesn't alleviate it. Choosing the wavelength of our self-defense laser requires higher

resolution that Fig. (II.B.1) can provide, so Figs. (II.B.4a-c) are included for more detail [Ref. 10].

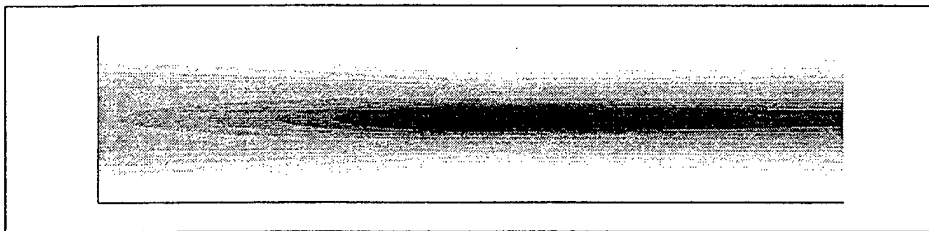


Figure II.B.3. Laser beam path with thermal blooming.

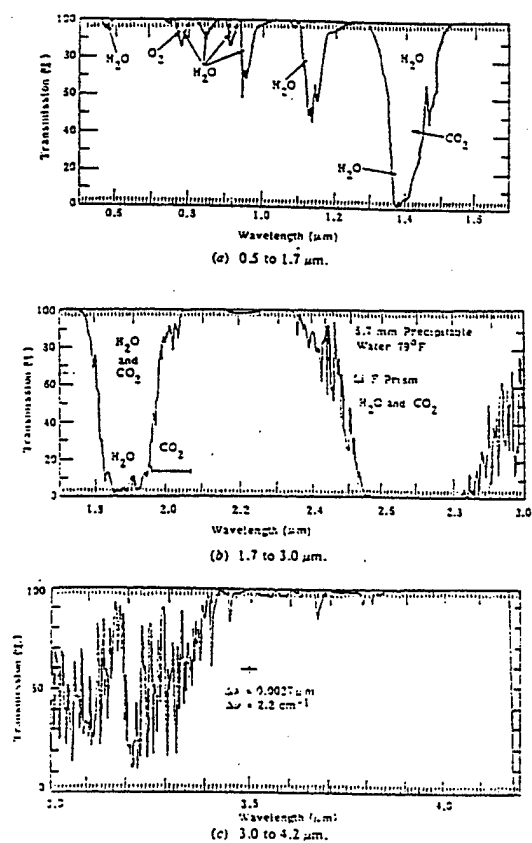


Figure II.B.4a-c. Atmospheric transmission. From Ref [10].

Many powerful lasers emit several wavelengths. For example, the MIRACL's nominal output wavelength is 3.8 μm , but it actually produces various laser lines around this wavelength. From Fig. (II.B.3), the transmittance values for 3.8 μm show a transmittance in the proximity of 90%, but the combined transmittance at the other wavelengths could quite possibly cause thermal blooming. The FEL provides a tunable wavelength that can be selected to a preferred transmittance to minimize thermal blooming.

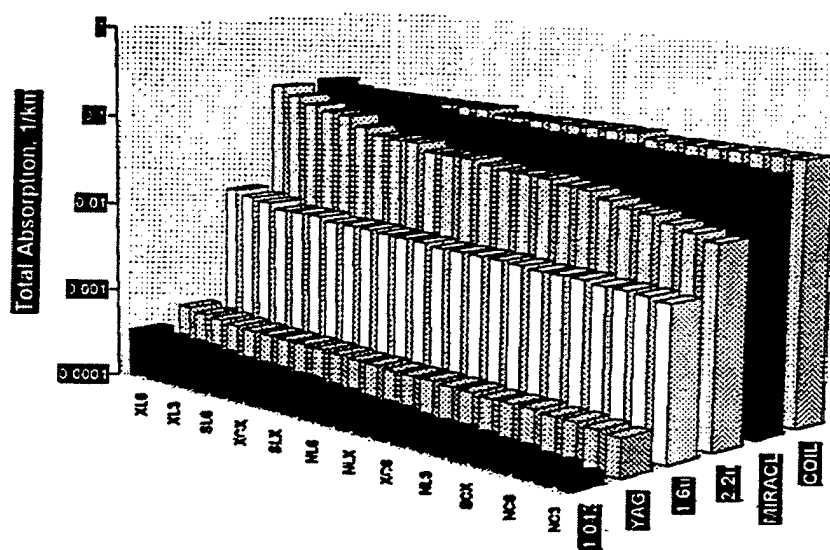


Figure II.B.5. Total absorption. From Ref [11].

Cook and Albertine computed the absorption coefficients for various lasers seen in Fig. (II.B.5) appropriate to a high-energy laser weapon system (HELWS) for deployment in a maritime environment [Ref. 11]. The graph shows the comparison of computer simulated absorption coefficients for the different wavelengths selected. Of the lasers selected, optimal transmittance was found to be at a wavelength of 1.042 μm . The

MIRACL's laser line, 3.8 μm , showed a significantly higher absorption than other lasers under maritime conditions.

Cook and Albertine took their computer simulation a step further by calculating the total extinction coefficients for the same laser lines shown in Fig. (II.B.6). Eye safety restrictions were also considered. Since it is tunable, the FEL could easily produce the optimal wavelength of 1.6 μm defined by Cook and Albertine.

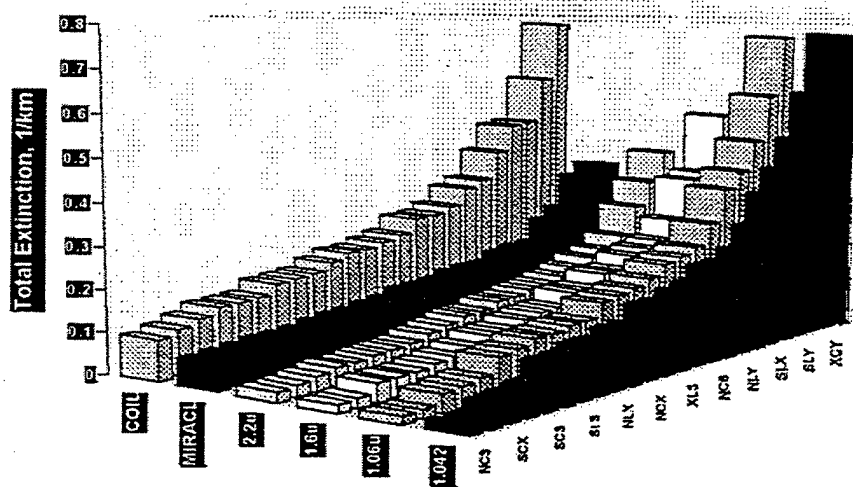


Figure II.B.6. Total extinction coefficients. From Ref [11].

III. FEL THEORY

A. BASIC OPERATION

The building blocks of an FEL are an accelerator, an undulator, and an optical cavity. The accelerator, or electron gun, generates a beam of relativistic electrons. These electrons exit the gun with relativistic energy, γmc^2 , where γ is the Lorentz factor, m is the electron rest mass and c is the speed of light. The beam of electrons enters the optical cavity in a long series of microbunches, while the laser pulses are bounced back and forth between two mirrors. The undulator is a series of alternating magnets that cause the interaction between the laser light and electron beam.

Figure (III.A.1) shows the undulator length, $L = N\lambda_0$, where N is the number of undulator periods and λ_0 is the undulator wavelength. The undulator is comprised of magnets arranged in order to produce a spatially periodic magnetic field, shown by the up and down arrows. This magnetic field causes the relativistic electrons to "wobble" in the transverse direction as they pass through the optical cavity. A semitransparent mirror allows 1-10% of the optical field power to be extracted from the optical cavity as

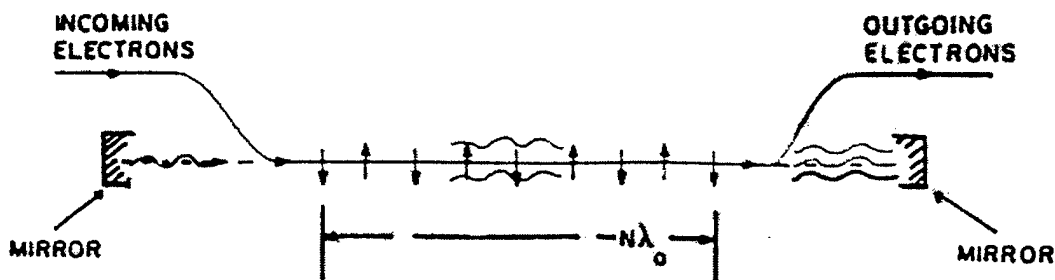


Figure III.A.1. Basic undulator configuration.

coherent electromagnetic radiation.

Laser light amplification depends on the interaction of the optical wave, the electron beam, and the spatially periodic magnetic field. The microbunches emitted from the electron gun travel at speed, $\beta_z c$, where β_z is the axial component of the velocity and c is the speed of light. As the microbunches traverse the undulator, they accelerate under the influence of the magnets in the transverse direction. The electrons interact strongly with the optical field only if they satisfy the resonance condition. The resonance condition will be satisfied if exactly one wavelength of light passes over one electron every time the electron traverses exactly one undulator wavelength [Ref. 12]. The resonance condition that relates the electron energy, λ , and λ_o can be expressed as

$$\lambda = \frac{(1 + K^2)\lambda_o}{2\gamma^2}, \quad (\text{III.A.1})$$

where the undulator parameter is introduced as $K = eB\lambda_o/2\pi mc^2$ and γ is the relativistic Lorentz factor. We will show how the undulator parameter is derived in the Pendulum Equation section. This equation shows the ability of the FEL to change its wavelength, λ , by changing the electron beam energy, γmc^2 , or the undulator characteristics, λ_o or K .

B. PENDULUM EQUATION

The transfer of energy from the electron beam to the optical beam takes place along the undulator. The magnetic field of a helically polarized undulator is represented as

$$\vec{B}_u = (B_x, B_y, B_z) = B(\cos(k_o z), \sin(k_o z), 0), \quad (\text{III.B.1})$$

where $k_o = 2\pi/\lambda_o$ and the z direction is along the undulator axis. The magnetic and electric fields of the optical wave in the resonator, are represented by

$$\vec{B}_r = B(\sin(\Psi), \cos(\Psi), 0), \quad (\text{III.B.2})$$

$$\vec{E}_r = E(\cos(\Psi), \sin(\Psi), 0), \quad (\text{III.B.3})$$

where $\Psi = kz - \omega t + \phi$, ω is the radial frequency, $k = 2\pi/\lambda$ is the wave number and ϕ is the optical phase.

We need to determine the significant forces present in the undulator to describe the motion of the electron. We start with the relativistic Lorentz force equations,

$$\frac{\partial(\gamma\vec{\beta})}{\partial t} = -\frac{e}{mc} [\vec{E}_r + \vec{\beta} \times (\vec{B}_r + \vec{B}_u)], \quad (\text{III.B.4})$$

$$\dot{\gamma} = -\frac{e}{mc} \vec{\beta} \cdot \vec{E}_r, \quad (\text{III.B.5})$$

$$\gamma^{-2} = 1 - \vec{\beta}^2, \quad (\text{III.B.6})$$

where $\dot{\gamma} = d\gamma/dt$. By substituting the undulator and the optical fields, into the Lorentz force equations, we obtain

$$\frac{\partial(\gamma\bar{\beta}_\perp)}{\partial t} = -\frac{e}{mc} [E(1-\beta_z)(\cos(\Psi), -\sin(\Psi), 0) + B\beta_z(-\sin(k_o z), \cos(k_o z), 0)], \quad (\text{III.B.7})$$

$$\frac{\partial(\gamma\bar{\beta}_z)}{\partial t} = -\frac{e}{mc} [E(\beta_x \cos(\Psi) - \beta_y \sin(\Psi)) + B(\beta_x \sin(k_o z), \beta_y \cos(k_o z))], \quad (\text{III.B.8})$$

$$\dot{\gamma} = -\frac{e}{mc} E [\beta_x \cos(\Psi) - \beta_y \sin(\Psi)]. \quad (\text{III.B.9})$$

For relativistic electrons, the E term in Eq. (III.B.7) is negligible compared to the $B\beta_z$ term since $E(1-\beta_z) \ll B\beta_z$ for $\gamma \gg 1$. Therefore, we include only the transverse force of the undulator, which gives us

$$\frac{\partial(\gamma\bar{\beta}_\perp)}{\partial t} = -\frac{e}{mc} B\beta_z(-\sin(k_o z), \cos(k_o z), 0). \quad (\text{III.B.10})$$

By integrating with respect to time, we acquire

$$\bar{\beta}_\perp = -\frac{K}{\gamma}(\cos(k_o z), \sin(k_o z), 0), \quad (\text{III.B.11})$$

where the undulator parameter is $K = eB\lambda_o/2\pi mc^2$. For $\gamma \gg 1$, $\beta_\perp \ll 1$. By inserting $\bar{\beta}_\perp$ into Eq. (III.B.9), we obtain

$$\dot{\gamma} = \frac{eEK}{\gamma mc} \cos(\zeta + \phi), \quad (\text{III.B.12})$$

where the electron phase is $\zeta = (k+k_o)z - \omega t$. For $t = 0$, the initial value for the electron phase is $\zeta(0) = \zeta_o = (k+k_o)z_o$. For relativistic electrons $k \gg k_o$ so that $\zeta_o \cong kz_o = 2\pi z_o/\lambda$. Thus, the electron phase, ζ , measures the z position with respect to an optical wavelength, λ .

Now we use $\bar{\beta}_\perp$ in Eq. (III.B.6) to obtain

$$\gamma^{-2} = 1 - \bar{\beta} \cdot \bar{\beta} = 1 - \beta_z^2 - \beta_\perp^2 = 1 - \beta_z^2 - K^2/\gamma^2, \text{ or } (1 + K^2)\gamma^{-2} = 1 - \beta_z^2. \quad (\text{III.B.13})$$

Taking the time derivative, we relate $d\gamma/dt$ and $d\beta/dt$

$$\frac{\dot{\gamma}}{\gamma} = \frac{\gamma^2 \beta_z \dot{\beta}_z}{(1 + K^2)}. \quad (\text{III.B.14})$$

Taking the first and second time derivative of the electron phase, ζ , we obtain

$$\dot{\zeta} = (k + k_o)c\beta_z - \omega, \text{ and} \quad (\text{III.B.15})$$

$$\ddot{\zeta} = (k + k_o)c\dot{\beta}_z. \quad (\text{III.B.16})$$

Solving Eq. (III.B.16) for $\dot{\beta}_z$ and substituting it into equation (III.B.14), we get

$$\frac{\dot{\gamma}}{\gamma} = \frac{\gamma^2 \beta_z \ddot{\zeta}}{(1 + K^2)(k + k_o)c}. \quad (\text{III.B.17})$$

For relativistic electrons with $\beta_z \cong 1$ and $k \gg k_o$, Eq. (III.B.17) reduces to

$$\frac{\dot{\gamma}}{\gamma} = \frac{\ddot{\zeta}}{2\omega_o}, \quad (\text{III.B.18})$$

where $\omega_o = \omega(1 + K^2)/2\gamma^2$, $\omega_o = k_o c$, and $\omega = kc$. We now solve for $\ddot{\zeta}$ in Eq. (III.B.18) and

substitute $\dot{\gamma}$ from Eq. (III.B.14) to obtain the electron equation of motion

$$\ddot{\zeta} = \frac{2\omega_o \dot{\gamma}}{\gamma} = \frac{2eKE\omega_o}{\gamma^2 mc} \cos(\zeta + \phi). \quad (\text{III.B.19})$$

Define a dimensionless time, $\tau = ct/L$, a dimensionless complex optical field $a =$

$|a|e^{i\phi}$ where $|a| = 4\pi eNKL|E|/\gamma^2 mc^2$, so that the electron equation of motion is in the

form of the pendulum equation

$$\ddot{\zeta} = |a| \cos(\zeta + \phi), \quad (\text{III.B.20})$$

where $(\dot{\dots}) = d(\dots)/d\tau$. Note that, $\ddot{\zeta}$ is positive when $-\pi/2 < \cos(\zeta + \phi) < \pi/2$ and

negative when $\pi/2 < \cos(\zeta + \phi) < 3\pi/2$. Some electrons are accelerated ahead in the

beam and some are accelerated back. As a result, the electrons become bunched near phase $(\zeta + \phi) = \pi/2$ by the FEL interaction.

C. WAVE EQUATION

In the previous section, we showed that the pendulum equation produced the bunched electrons via the FEL interaction. We will now describe the interaction these bunched electrons have on the radiation field. Maxwell's inhomogeneous wave equation describes [Ref. 12] an optical vector potential $\vec{A}(\vec{r}, t)$ being driven by a current density \vec{J}_\perp ,

$$\left[\vec{\nabla}^2 - \frac{1}{c^2} \frac{\partial^2}{\partial t^2} \right] \vec{A}(\vec{r}, t) = -\frac{4\pi}{c} \vec{J}_\perp, \quad (\text{III.C.1})$$

where $\vec{\nabla}^2 = \partial^2 / \partial x^2 + \partial^2 / \partial y^2 + \partial^2 / \partial z^2$. The vector potential $\vec{A}(z, t)$ for a helical FEL is

$$\vec{A}(z, t) = \frac{c}{\omega} E(z, t) [\sin(kz - \omega t + \phi(z, t)), \cos(kz - \omega t + \phi(z, t)), 0], \quad (\text{III.C.2})$$

where the corresponding electric field \vec{E} is

$$\vec{E} = -\frac{1}{c} \frac{\partial \vec{A}}{\partial t} = E(z, t) [\cos(kz - \omega t + \phi(z, t)), -\sin(kz - \omega t + \phi(z, t)), 0]. \quad (\text{III.C.3})$$

The plane wave traveling in the z direction as in Eq. (III.C.2) has no x or y dependence so that Eq. (III.C.1) becomes

$$\left[\frac{\partial^2}{\partial z^2} - \frac{1}{c^2} \frac{\partial^2}{\partial t^2} \right] \vec{A}(\vec{r}, t) = -\frac{4\pi}{c} \vec{J}_\perp. \quad (\text{III.C.4})$$

The second derivative of the vector potential $\vec{A}(z, t)$ with respect to z is

$$\begin{aligned}
\frac{\partial^2}{\partial z^2} \bar{A} &= \frac{1}{k} \frac{\partial E}{\partial z} \left[k + \frac{\partial \phi}{\partial z} \right] [\cos(\Psi), -\sin(\Psi), 0] \\
&+ \frac{1}{k} \frac{\partial^2 E}{\partial z^2} [\sin(\Psi), \cos(\Psi), 0] + \frac{1}{k} \frac{\partial E}{\partial z} \left[k + \frac{\partial \phi}{\partial z} \right] [\cos(\Psi), -\sin(\Psi), 0] \\
&+ \frac{E}{k} \frac{\partial^2 \phi}{\partial z^2} [\cos(\Psi), -\sin(\Psi)] + \frac{E}{k} \left[k + \frac{\partial \phi}{\partial z} \right]^2 [-\sin(\Psi), -\cos(\Psi)]. \quad (\text{III.C.5})
\end{aligned}$$

Assuming the amplitudes and phases vary slowly with respect to time and distance traveled along the z axis is expressed as $\partial E/\partial z \ll kE$, $\partial \phi/\partial z \ll k\phi$, $\partial E/\partial t \ll \omega E$, and $\partial \phi/\partial t \ll \omega \phi$, where $\omega = kc$. Thus, E and ϕ vary slowly allowing us to neglect the second-order derivatives in Eq. (III.C.5) simplifying it to

$$\frac{\partial^2}{\partial z^2} \bar{A} \cong 2 \frac{\partial E}{\partial z} [\cos(\Psi), -\sin(\Psi), 0] + E(k + 2 \frac{\partial \phi}{\partial z}) [-\sin(\Psi), -\cos(\Psi), 0]. \quad (\text{III.C.6})$$

Taking the second time derivative of the vector potential $\bar{A}(z, t)$ gives

$$\begin{aligned}
\frac{\omega}{c} \frac{\partial^2}{\partial t^2} \bar{A} &= \frac{\partial E}{\partial t} \left[\frac{\partial \phi}{\partial t} - \omega \right] [\cos(\Psi), -\sin(\Psi), 0] + \frac{\partial E^2}{\partial t^2} [\sin(\Psi), \cos(\Psi), 0] \\
&+ \frac{\partial E}{\partial t} \left[\frac{\partial \phi}{\partial t} - \omega \right] [\cos(\Psi), -\sin(\Psi), 0] + E \frac{\partial \phi^2}{\partial t^2} [\cos(\Psi), -\sin(\Psi), 0] \\
&+ E \left[\frac{\partial \phi}{\partial t} - \omega \right]^2 [-\sin(\Psi), -\cos(\Psi), 0]. \quad (\text{III.C.7})
\end{aligned}$$

Again, the amplitudes and phases are both slowly-varying so we can ignore second-order derivatives and Eq. (III.C.7) becomes

$$\frac{1}{c^2} \frac{\partial^2}{\partial t^2} \bar{A} \cong -2 \frac{1}{c} \frac{\partial E}{\partial t} [\cos(\Psi), -\sin(\Psi), 0] + \frac{1}{c} \left(\omega E - 2E \frac{\partial \phi}{\partial t} \right) [-\sin(\Psi), -\cos(\Psi), 0]. \quad (\text{III.C.8})$$

Substituting Eqs. (III.C.6) and (III.C.8) into Eq. (III.C.4) gives

$$\left[\nabla^2 - \frac{1}{c^2} \frac{\partial^2}{\partial t^2} \right] \vec{A} \cong 2 \left[\frac{\partial E}{\partial z} + \frac{1}{c} \frac{\partial E}{\partial t} \right] [\cos(\Psi), \sin(\Psi), 0] + 2E \left[\frac{\partial \phi}{\partial z} + \frac{1}{c} \frac{\partial \phi}{\partial t} \right] [-\sin(\Psi), -\cos(\Psi), 0]. \quad (\text{III.C.9})$$

We again define a dimensionless time as $\tau = ct/L$, and define a new position $z \rightarrow z + ct$, using chain rule to simplify the operator, Eq. (III.C.9) becomes

$$\left[\nabla^2 - \frac{1}{c^2} \frac{\partial^2}{\partial t^2} \right] \vec{A} \cong 2 \left[\frac{1}{L} \frac{\partial E}{\partial \tau} \right] [\cos(\Psi), \sin(\Psi), 0] + 2E \left[\frac{1}{L} \frac{\partial \phi}{\partial \tau} \right] [-\sin(\Psi), -\cos(\Psi), 0] \quad (\text{III.C.10})$$

which, combined with Eq. (III.C.4) yields

$$2 \left[\frac{1}{L} \frac{\partial E}{\partial \tau} \right] [\cos(\Psi), \sin(\Psi), 0] + 2E \left[\frac{1}{L} \frac{\partial \phi}{\partial \tau} \right] [-\sin(\Psi), -\cos(\Psi), 0] \approx -\frac{4\pi}{c} \vec{J}_\perp. \quad (\text{III.C.11})$$

By definition, the current density for a single electron is $\vec{J}_\perp = -ec\vec{\beta}_\perp$. Using $\vec{\beta}_\perp$, we obtain

$$\vec{J}_\perp = \frac{ecK}{\gamma} [\cos(k_o z), \sin(k_o z), 0], \quad (\text{III.B.12})$$

where K is the undulator parameter, k_o is the undulator wave number, and γ is the Lorentz factor. Substituting Eq. (III.C.12) into Eq. (III.C.11) gives

$$2 \left[\frac{1}{L} \frac{\partial E}{\partial \tau} \right] [\cos(\Psi), \sin(\Psi), 0] + 2E \left[\frac{1}{L} \frac{\partial \phi}{\partial \tau} \right] [-\sin(\Psi), -\cos(\Psi), 0]. \quad (\text{III.C.13})$$

Equation (13) is divided into two orthogonal unit vectors describing the evolution of $\partial E / \partial \tau$ and $\partial \phi / \partial \tau$.

$$\begin{aligned}\frac{\partial E}{\partial \tau} &= -\frac{2\pi e L K}{\gamma} [\cos(k_o z), \sin(k_o z), 0] \cdot [\cos(\Psi), \sin(\Psi), 0]. \\ &\cong -\frac{4\pi e K}{\gamma} [\cos(k_o z), \sin(k_o z), 0].\end{aligned}\quad (\text{III.C.14})$$

Projecting out each of the orthogonal components gives

$$\frac{\partial E}{\partial \tau} = -\frac{2\pi e L K}{\gamma} \cos(\zeta + \phi), \quad (\text{III.C.15})$$

where ζ is the electron phase $(k+k_o)z - \omega t$ and

$$\frac{\partial \phi}{\partial \tau} = \frac{2\pi e L K}{\gamma} \sin(\zeta + \phi). \quad (\text{III.C.16})$$

Equations (III.C.15) and (III.C.16) are the amplitude and phase components of the wave equation driven by a single electron. The FEL electron current is a sum over many sampled electrons, denoted by $\langle \dots \rangle$, and multiplied by the electron particle density, ρ , so that the wave equation for the FEL becomes

$$\frac{\partial E}{\partial \tau} = -\frac{2\pi e \rho L K}{\gamma} \langle \cos(\zeta + \phi) \rangle, \quad (\text{III.C.17})$$

$$\frac{\partial \phi}{\partial \tau} = \frac{2\pi e \rho L K}{\gamma} \langle \sin(\zeta + \phi) \rangle. \quad (\text{III.C.18})$$

Combining Eqs. (III.C.17) and (III.C.18) and using the complex dimensionless optical field $a = |a|e^{i\phi}$, where $|a| = 4\pi e N K L |E|/\gamma^2 m c^2$, we have

$$\frac{\partial a}{\partial \tau} = \dot{a} = -j \langle e^{-i\zeta} \rangle, \quad (\text{III.C.19})$$

where the dimensionless current is $j = 8\pi^2 e^2 \rho N K^2 L^2 / \gamma^3 m c^2$. The optical field is directly dependent on the dimensionless current, j , and the electron phase average $\langle e^{-i\zeta} \rangle$.

IV. LASER MATERIAL INTERACTION

A. BACKGROUND

This chapter discusses the laser-matter interaction, when the laser beam energy impacts the sample material. Does the laser burn through the material? Does the material absorb the energy and diffuse it through the material? Experiments and analogies will give the answers to these questions. Research and calculation will help us understand the laser damage process so as to introduce scaling to a larger full-scale model.

B. THERMAL DIFFUSION LENGTH

The thermal diffusion length, D , characterizes a material's ability to absorb and transport heat. If this length is longer than the incoming laser's spot size diameter, d , the material is better able to diffuse the laser beam's incident energy faster than the incoming energy can melt the material. To make a simple analogy, consider trying to fill a sink with water when the drain is not plugged. With the faucet on high, the drain can take away enough water so that the net flow of water into the sink is negative and the sink never gets full. In the same manner, the sample material can diffuse the incident energy away faster than the energy can melt the material.

Schriempf [Ref. 13] derives the thermal diffusion length. We start with the classical heat flow equation,

$$\rho C \frac{\partial T}{\partial t} = K \nabla^2 T + A, \quad (\text{IV.B.1})$$

where $\nabla^2 = \frac{\partial^2}{\partial x^2} + \frac{\partial^2}{\partial y^2} + \frac{\partial^2}{\partial z^2}$, ρ is density, C is specific heat, T is temperature, t is time,

K is thermal conductivity and A is the heat produced per unit volume per unit time. This equation relates the rate of heat deposition into a volume element, $dx dy dz$, to the rate of heat production plus the net flow of heat across the faces of the volume element.

The main interest lies in the energy deposited in the z direction. Energy flow in the x and y directions is disregarded, assuming the dimensions of the volume element used do not allow thermal diffusion in those directions. With this assumption, Eq.

(IV.B.1) becomes

$$\rho C \frac{\partial T}{\partial t} = K \left(\frac{\partial^2 T}{\partial z^2} \right) + A. \quad (\text{IV.B.2})$$

Since, ρ , C and K are constants, they are grouped together to introduce a new constant κ ,

the thermal diffusivity, where $\kappa = \frac{K}{\rho C}$. Using this definition, we rearrange Eq. (IV.B.2)

as

$$\frac{\partial^2 T}{\partial z^2} - \frac{1}{\kappa} \frac{\partial T}{\partial t} = -\frac{A}{K}. \quad (\text{IV.B.3})$$

Since absorption is large for metals, A is practically zero at depths just beyond the surface, and Eq. (IV.B.3) becomes

$$\frac{\partial^2 T}{\partial z^2} - \frac{1}{\kappa} \frac{\partial T}{\partial t} = 0, \quad (\text{IV.B.4})$$

where solutions to this equation take the form

$$T(z, t) = \frac{2F_o \sqrt{\kappa t}}{K} \text{ierfc}[z / 2\sqrt{\kappa t}], \quad (\text{IV.B.5})$$

where F_o is the initial power density, t is time, $ierfc(x) = \frac{1}{\sqrt{\pi}} e^{-x^2} - x + erf(x)$, and

$$erf(x) = \frac{2}{\sqrt{\pi}} \int_0^x e^{-l^2} dl.$$

Schriempf defines the thermal diffusion length, D , as the distance required for the temperature to drop to $1/e$ of its initial value where

$$D = 2\sqrt{\kappa\tau}, \quad (IV.B.6)$$

where τ is the time needed to raise the material's temperature from ambient to melting (ΔT) and is defined as

$$\tau = \frac{\pi K^2 \Delta T^2}{4 F_o^2 \kappa}. \quad (IV.B.7)$$

When the thermal diffusion length is greater than the laser beam's spot size diameter ($D > d$), the heat deposited by the laser beam will be diffused away by the material in less time than it takes the material to melt. When $D < d$, the heat deposited is sufficient to cause melting of the material, as in the sink analogy: the drain allows less water to escape so that the net flow of water into the sink is positive and it gets full.

We calculated the thermal diffusion length for 6061 Aluminum where $D = 1.79$ mm. At TJNAF, a sample of 6061 Aluminum was irradiated with a spot diameter of $d = 1$ mm for several minutes and as expected, the sample did not melt because $d < D$. For a later experiment, TJNAF irradiated the 6061 Aluminum with a laser spot size $d = 2$ mm and since $d > D$, the laser beam was able to burn through the sample within seconds.

C. SCALING

Scaling is an important process to understand in order for us to properly use a small 100 W laser to estimate the damage from a larger laser weapon. The thermal diffusion length of the sample can scale the laser beam's spot size diameter accordingly to mitigate the heat loss. Scaling is important because currently there isn't a megawatt (MW) class FEL available. It would cost significantly more to build such a laser just for tests.

Albertine and Cook state that a power density of 10 kW/cm^2 over an area of 100 cm^2 is required to destroy a missile. The total power required is 1 MW. Only one laser in the world operates at this power level. Currently, there are no FELs with this amount of power. The FEL at TJNAF leads the field with a maximum power output of 710 W and they are currently undergoing upgrades to obtain 20 kW in the next few years.

Using $\Phi = 10 \text{ kW/cm}^2$ and $P = 710 \text{ W}$, TJNAF can produce a spot size of 0.071 cm^2 , correlating to a diameter of 3 mm. By scaling the spot size to this, we maintain the power density required by Albertine and Cook and we can study the effects of a megawatt laser without paying for it.

Aluminum is more conductive than the samples that we studied. We can assume that the thermal diffusion lengths of the tested samples will be less. As such, the effects of thermal diffusion should be drastically reduced for our experiments.

V. LASER DAMAGE TO MATERIAL

A. BACKGROUND

Laser damage to material has been studied since the mid-1970's. Several Department of Defense and civilian agencies have used various lasers to determine the damage to different materials. While laser damage to materials is not a new subject, using an FEL to incur damage is new. This chapter will describe the TJNAF FEL, the user laboratories there, and the experimental procedures for damaging materials. It will also discuss the experimental data taken.

B. THOMAS JEFFERSON NATIONAL ACCELERATOR FACILITY

The Thomas Jefferson National Accelerator Facility's (TJNAF) Free Electron Laser (FEL) is located in Newport News, Virginia. It is an U.S. Department of Energy (DOE) facility that is operated and maintained by the Southeastern Universities Research Association (SURA), Incorporated. The TJNAF FEL first lased on June 15, 1998, and two days later, it increased power output to 155 W of continuous wave power. By July 29, 1998, TJNAF increased the laser output power to 311 W, a "28-fold increase over any other FEL" [Ref. 7]. On March 11, 1999, TJNAF further increased the output power to 710 watts while recirculating the electron beam. The TJNAF FEL is now the most powerful FEL in the world. With upgrades, the TJNAF FEL power output will be increased to 20 kW in the near future. With research and development, it may be possible for a megawatt-class FEL to soon be realized.

Figure (V.B.1) is a basic diagram of the current FEL configuration at TJNAF and Figure (V.B.2) shows the modifications that will boost the output power to allow for a 20 kW infrared wavelength laser, or a 1 kW ultraviolet wavelength laser [Ref. 7].

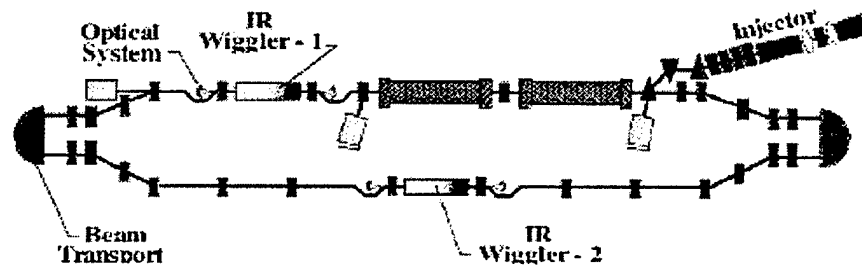


Figure V.B.1. Current FEL configuration.

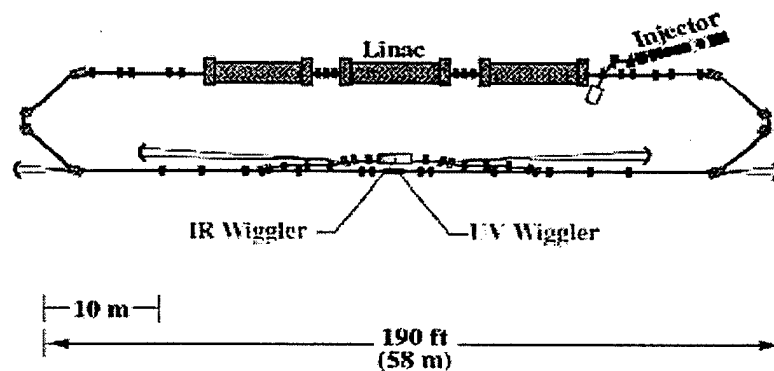


Figure V.B.2. Upgraded FEL configuration.

C. USER LAB

Once the FEL beam is produced, it can be transferred to several user laboratories via a low-loss optical path for various applications. The damage experiments described in this thesis were conducted in user laboratory number one. Various TJNAF personnel operated the equipment to conduct the experiments; included were Michelle Shinn, Steve Benson and George Neil. Figure (V.C.1) is a picture of the optical bench set-up used for experiments. The set-up included a focusing calcium fluoride lens, a sample holder, an iris and a power meter. In Fig. (V.C.1), the number 1 corresponds to the lens. The sample holder is not shown in the picture but its position on the bench set up is denoted by the line numbered 2. The line numbered 3 is the focus of the lens. Object 4 is an iris. Its purpose will be explained in a later section. The power meter will be shown in a later picture. Two video cameras were set up to record the experiments, one in front of the sample holder and one behind.

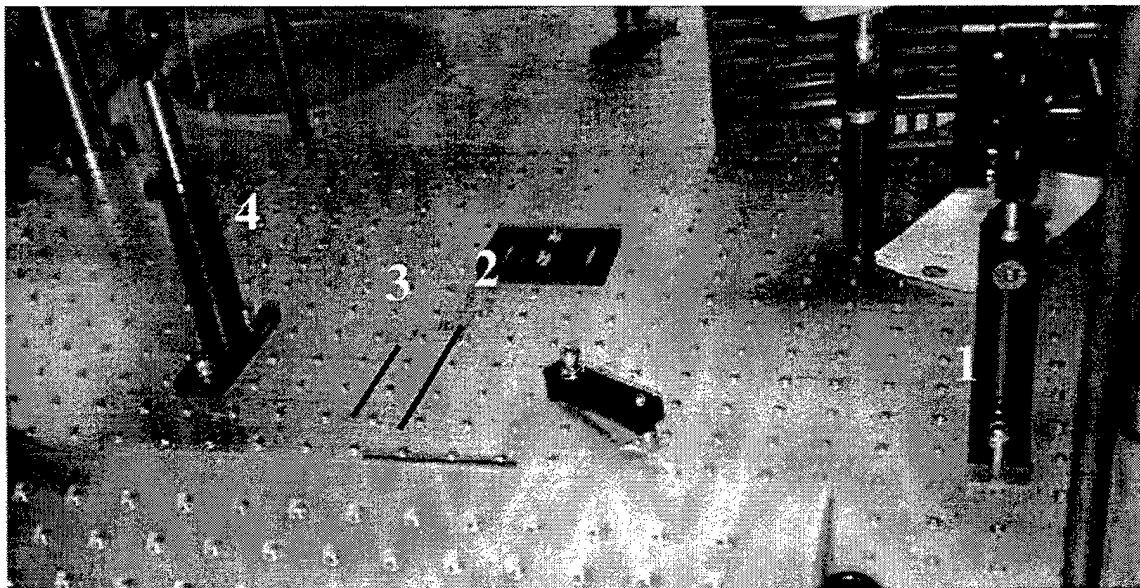


Figure V.C.1. Optical bench.

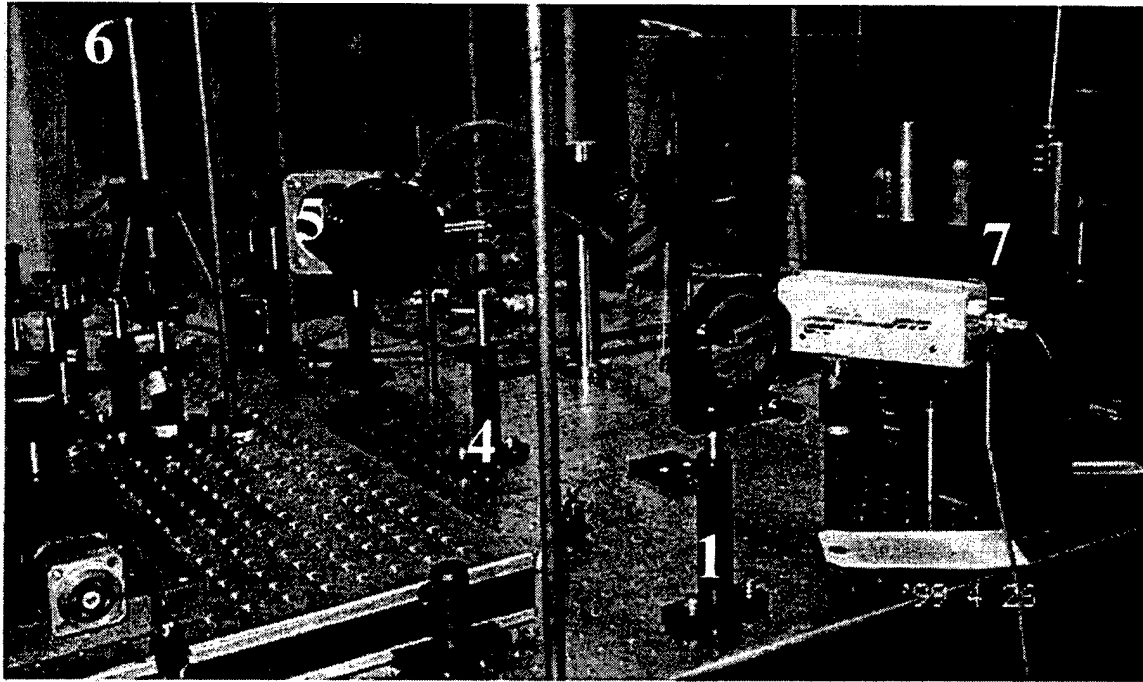


Figure V.C.2. Front view of optical bench.

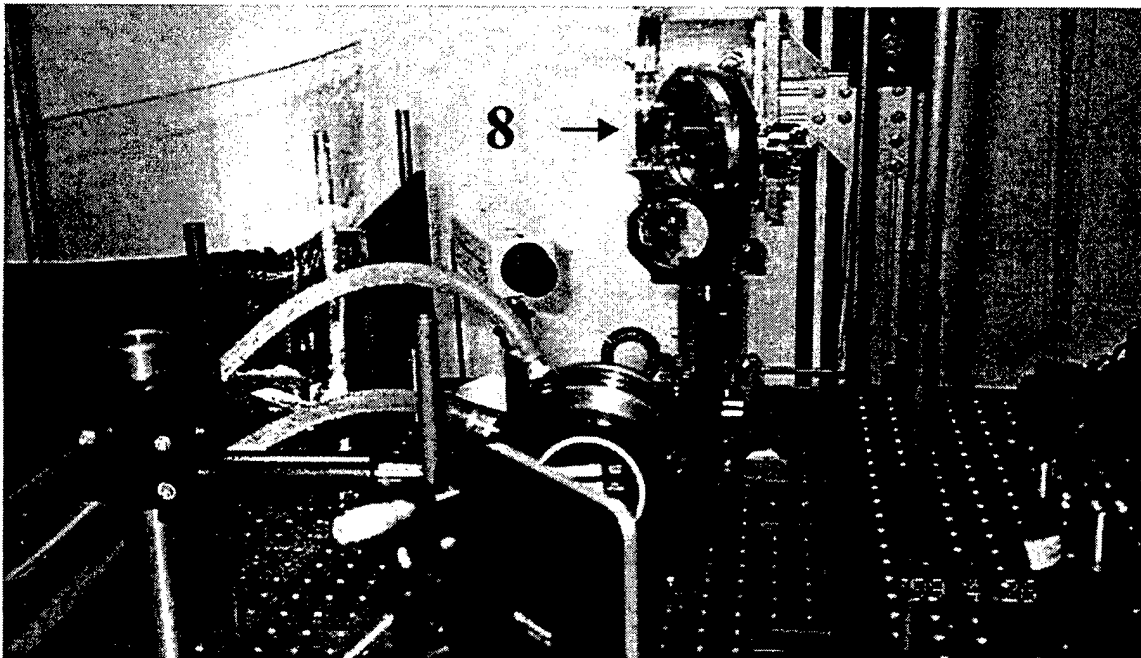


Figure V.C.3. Rear view of optical bench.

Figure (V.C.2) is the front view of the optical bench. The number 1 correlates to the lens, as before. The number 5 shows the power meter's location. Numbers 6 and 7 show the positions of the back and front video cameras respectively. Figure (V.C.3) is a rear view of the optical bench. The number 8 shows the output of the transfer equipment used to transfer the FEL beam to the user laboratory.

D. EXPERIMENTAL PROCEDURES

All samples were irradiated with the FEL laser beam at a wavelength of 4.825 μm . Two pulse repetition frequencies (PRF) were used; 74.85 MHz for the phenolic resin sample and 37.425 MHz for the pyroceram sample. The power meter in the user laboratory measured the average powers for each sample's run; it was 100 W for phenolic resin and 103 W for pyroceram.

To acquire the desired irradiance of 10 kW/cm², the laser beam was focused through a calcium fluoride lens with a focal length of 300 mm. At the focal point, denoted in Fig. (V.C.1) by the line numbered 3, the minimum beam radius was 80 μm . Michelle Shinn, of TJNAF, used a beam propagation computer code, PARAXIA, to model the beam. Using PARAXIA, it was determined that for the required irradiance of 10 kW/cm², the target materials should be placed 26 mm in front of the focus. This position is denoted by the line numbered 2 in Fig (V.C.1). Beam burn-through was determined by observing the signals on the power meter placed behind the targets, and by watching for coherent harmonics on an iris, denoted by the number 4 in Figs (V.C.1) and (V.C.2), which was placed 15 cm behind the target [Ref. 14].

E. PHENOLIC RESIN EXPERIMENTS

Phenolic resin samples were obtained from CAPT Powell, USN, an instructor at the Naval Postgraduate School. Two phenolic resin samples were irradiated; one on March 9 referred to as Phenolic Sample 1 and the other on March 12 referred to as Phenolic Sample 2.

1. Phenolic Sample 1

Phenolic Sample 1 is circular with a diameter of 32.5 mm and a 7.1 mm hole in the middle. It varies in thickness from 1.6 mm to 3.2 mm. Figure (V.E.1.1) is a picture of Sample 1 after 3 irradiations, with the sample rotated 90° counterclockwise after each run. In Fig. (V.E.1.1), the numbers correspond to the data in Table (V.E.1.1). The power meter in the lab indicated a power of 100 W incident on the sample. The FEL pulse repetition frequency was 74.85 MHz.

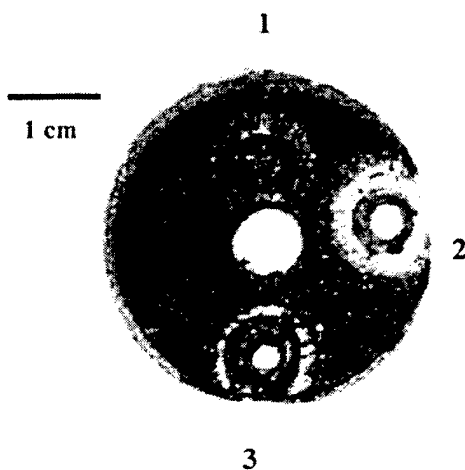


Figure V.E.1.1. Phenolic Sample 1.

Run #	Irradiances (kW/cm ²)	Thickness (mm)	Exposure Time (s)	Crater Depth (mm)	Estimated Burn Time (s)	Penetration Rate (mm/sec)	Burn thru?
1	10	1.6	3.4	0.1	3.4	0.029	No
2	10	2.5	11.7/ 26.5	2.5	7.4	0.34	Yes
3	10	3.2	13.5	3.2	7.9	0.41	Yes

Table V.E.1.1. Irradiation of Phenolic Sample 1.

For the first-ever FEL irradiations of sample material, the objectives were made simple: to see if the FEL would burn through the material by detecting at least 50% of the incident energy on the power meter behind the sample. Run number one did not achieve burn-through because of operator intervention. After initial irradiation, the rear camera showed that the sample had ignited. The FEL operators quickly stopped the experiment only to find that the sample had slightly charred on the reverse side and had not burned through. From the video, the burn time was approximated to be 3.4 seconds. The beam penetrated 0.1 mm of material in this burn time yielding a 0.029 mm/sec penetration rate.

For run number two, the sample was irradiated twice. Initially, the sample was irradiated for 11.7 seconds with an observed burn-through time of approximately 1.4 seconds. A second irradiation lasted 26.5 seconds. For run number three, the sample was irradiated for 13.5 seconds with a burn-through time of approximately 7.9 seconds.

Figure (V.E.1.2) shows the results of run number two, and is similar to run numbers one and three. The crater is tapered with a slightly smaller area on the back than on the front. There is a crater lip approximately 1 mm high built up from the damaged material and debris. The presence of the white crust probably stems from the separation of the resin into its elements due to heating. Run number three has less crust and run number one has significantly less crust than run two, as seen in Fig. (V.E.1.1). Because run number two was irradiated twice, it has more white crust on its lip. The white crust and lips are also evident on the back side for runs two and three. Since run number one did not burn through, its crater was merely the protruding lip.

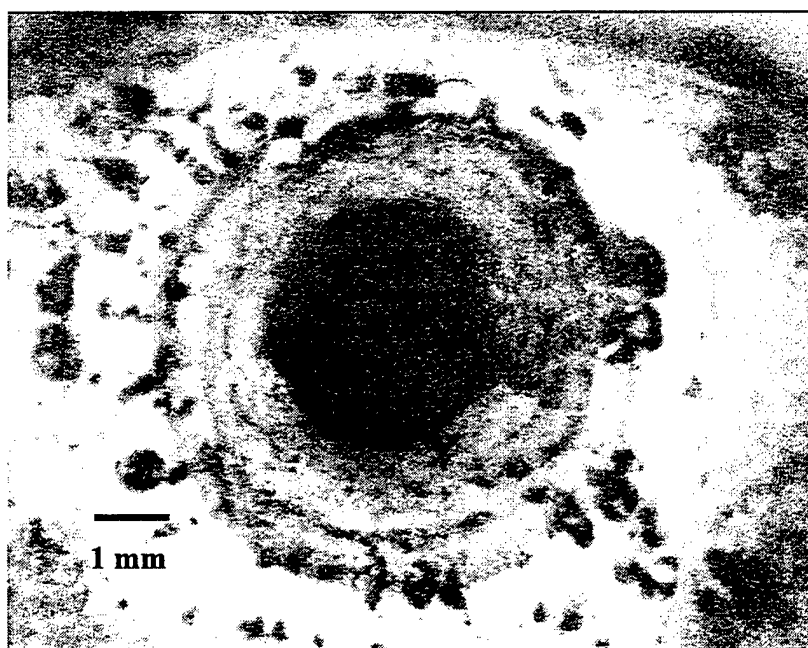


Figure V.E.1.2. Microscope picture of Phenolic Sample 1, run #2.

2. Phenolic Sample 2

Phenolic Sample 2 is circular with a diameter of 31.0 mm with a 7.1 mm hole in the middle. It varies in thickness from 1.5 mm to 3.8 mm. Figure (V.E.2.1) shows Sample 2 after 7 irradiations taken in counterclockwise order and numbered in Table (V.E.2.1). The incident power was 100 W with a pulse repetition rate of 74.85 MHz.

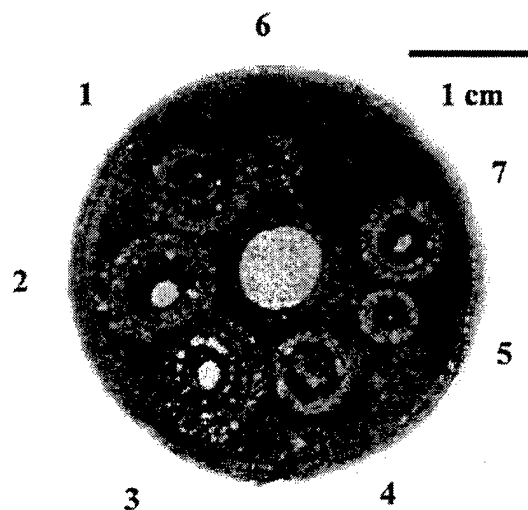


Figure V.E.2.1. Phenolic Sample 2.

Run #	Irradiances (kW/cm ²)	Thickness (mm)	Exposure Time (s)	Crater Depth (mm)	Estimated Burn Time (s)	Penetration Rate (mm/sec)	Burn thru?
1	12	3.8	1	3.0	1	3.0	No
2	12	2.2	2	2.2	1.4	1.57	Yes
3	12	1.7	3	1.7	1.0	1.7	Yes
4	12	1.6	0.5	1.6	0.5	3.2	No
5	680	1.5	1	1.4	< 0.06	> 20	Yes
6	680	3.2	2	3.2	< 0.06	> 50	Yes

Table V.E.2.1. Irradiation of Phenolic Sample 2.

All runs on sample number two produced a lip around the entrance of the cavities ranging from 0.1 mm to 1 mm in height. They also produced a white crust probably coming from some sort of elemental extract of the resin separated during heating. For the runs that did not burn through, one and four, a crater shaped like an inverted cone with a rounded apex was created. Inspection of the back side of run four showed charring, indicating that the beam almost burned through. Runs that achieved burn through had a tapered crater, with the back edge slightly smaller than the front. Lips formed on the reverse side of the sample, just like on the front side and surrounded by the white crust. Run number seven was a demonstration for another experiment.

Figure (V.E.2.2) shows the results of run number three and is representative of the runs with irradiance of 12 kW/cm², runs one through four. A crater is again formed with the white crust encircling the lip.

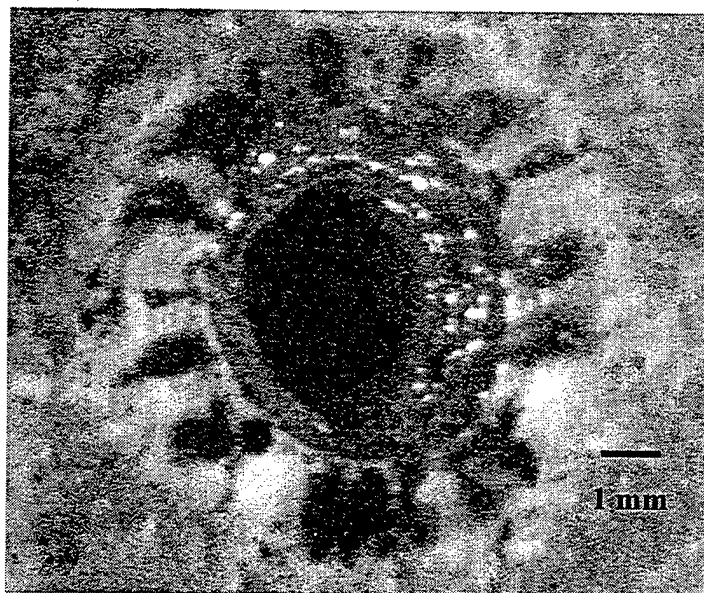


Figure (V.E.2.2). Microscope picture of Phenolic Resin Sample 2, run #3.

Figure (V.E.2.3) shows run six which is similar to the damage produced in run five. Both runs five and six had higher irradiance of 680 kW/cm^2 achieved by making the laser spot size smaller and results in a crater that is smaller by a factor of two or three. The beams with higher power density were able to punch through the material faster and produced a much smaller lip around the crater. The same white crust occurs on the surface, but in smaller amounts. Penetration rates are estimated in Table (V.E.2.1).

Data from Table (V.E.2.1) suggests that for low irradiance of 12 kW/cm^2 , the penetration rate decreases as the exposure time increases. This decline in recession rate could be due to smoke and debris flying out of the crater while the beam is burning through the phenolic material. The smoke and debris impede the laser from doing damage. TJNAF is planning future experiments with wind which might alleviate this

problem. Recession rates for the 680 kW/cm^2 irradiances suggests the recession rate increases with exposure time.

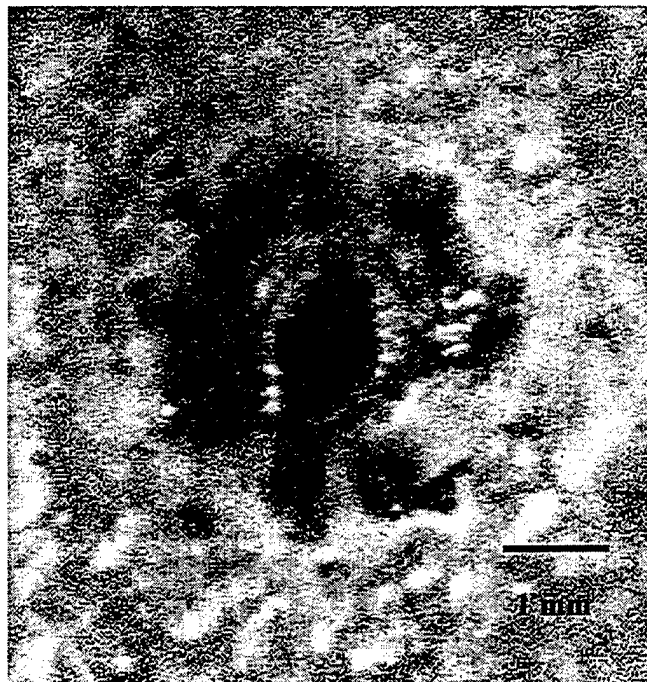


Figure V.E.2.3. Microscope picture of Phenolic Resin Sample 2, run #6.

F. PYROCERAM EXPERIMENTS

Pyroceram samples were provided by LCDR James Childs, USN, of the Naval Surface Warfare Center, Port Hueneme. The two pyroceram samples, Pyroceram Sample 1 and Pyroceram Sample 2, were irradiated on March 23, 1999 at TJNAF in user laboratory number one.

1. Pyroceram Sample 1

Pyroceram Sample 1 has an irregular shape with an average depth of 7 mm. Figure (V.F.1.1) shows Sample 1 after 3 irradiations, numbered from right to left, with the numbers correlating to the data in Table (V.F.1.1). The laser power was 103 Watts with a pulse repetition rate of 74.85 MHz at a wavelength of 4.83 μm .

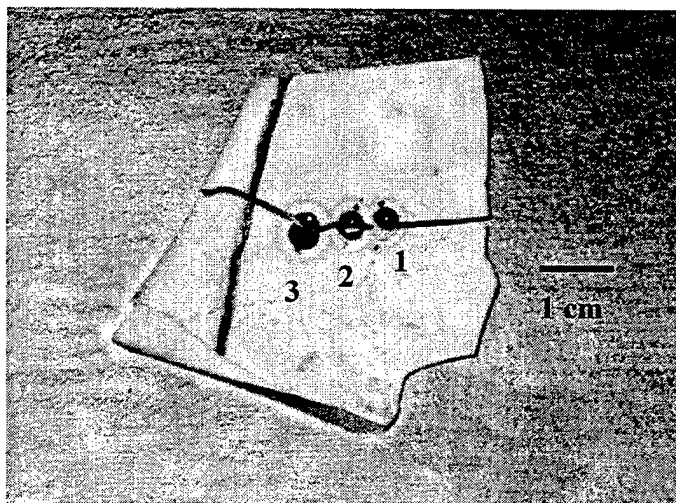


Figure V.F.1.1. Pyroceram Sample 1.

Run Number	Avg. Irradiance (kW/cm ²)	Exposure Time (s)
1	9	2
2	9	4
3	9	6

Table V.F.1.1. Irradiation of Pyroceram Sample 1.

Each irradiation of the sample caused a spray of sparks, flying debris and smoke. Run number three shattered five seconds into the six second irradiation period. After irradiation, there was molten pyroceramic material in each crater which cooled into the black glossy material seen in Fig. (V.F.1.1). The irradiations did not produce a noticeable lip as in the phenolic tests. Each of the crater's dimensions are detailed in Table (V.F.1.2), but the presence of the black glossy material prevented an accurate measurement of depths. The runs also produced a distinct circular ring around the craters. The origin of these rings is unknown, but they may be the result of material alteration due to heating. There were no notable marks on the back of the sample. The laser beam did not burn through sample 1 on any run, but the varied exposure times yielded craters with increasingly larger dimensions

Run Number	Crater Diameter (mm)	Depth (mm)	Ring Diameter (mm)
1	3	1	4.5
2	3	1.25	5
3	5	1.5	7.5

Table V.F.1.2 . Crater dimensions for Pyroceram Sample 1.

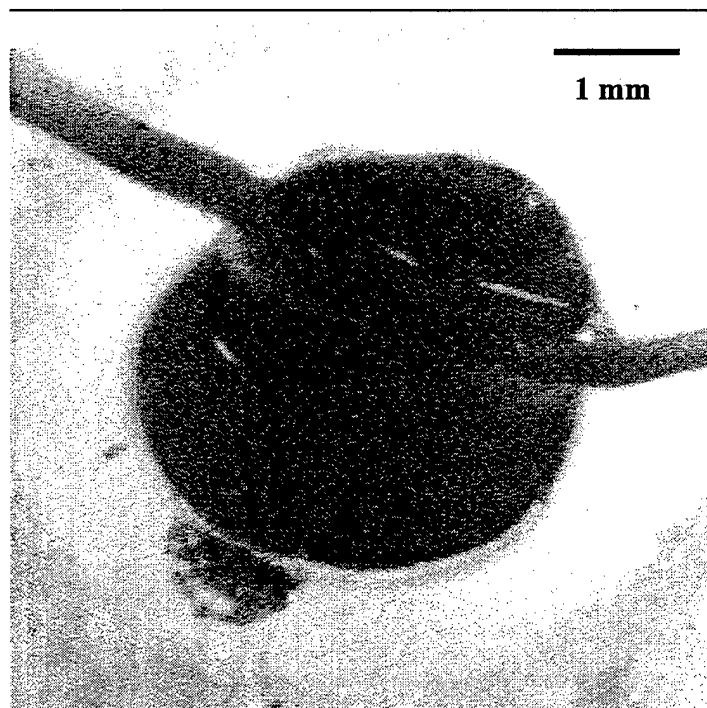


Figure V.F.1.2. Pyroceram Sample 1, run #3.

Figure (V.F.1.2) shows the crater formed on Pyroceram Sample 1, in Run 3 and is representative of the other runs. While runs one and two showed no signs of cracking or shattering, run three shattered five seconds into the six second irradiation period.

Stresses caused by the longer exposure time of run three and the earlier runs one and two probably contributed to the shattering in run three. Runs one and two are only separated by 10 mm and runs two and three are separated by only 5 mm. In the future, runs should be spaced further apart, or if possible have only one irradiation per sample.

2. Pyroceram Sample 2

Pyroceram Sample 2 has an irregular shape with an average depth of 7 mm. Figure (V.F.2.1) shows Sample 2 after three irradiations, numbered from right to left corresponding to the data in Table (V.F.2.1). The laser power was 103 W with a pulse repetition rate of 74.85 MHz at a wavelength of $4.83\text{ }\mu\text{m}$.

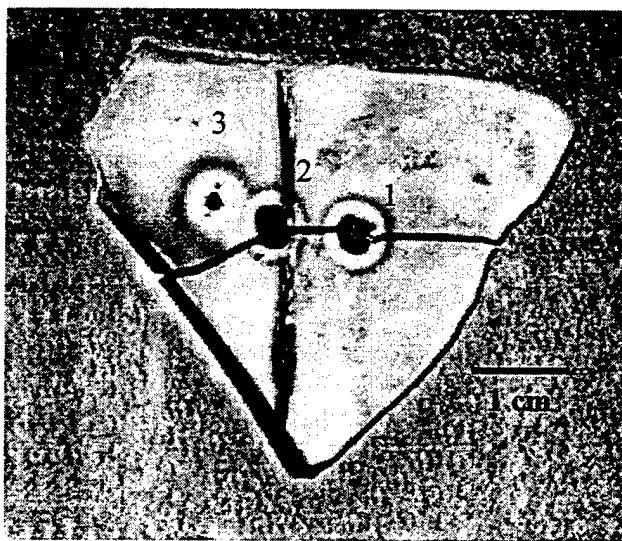


Figure V.F.2.1. Pyroceram Sample 2.

Run Number	Avg. Irradiance (kW/cm ²)	Exposure Time (s)	Comments
1	9	7	
2	9	7.5	Sample shattered. Irradiated after shattering.
3	500	11	

Table V.F.2.1. Irradiation of Pyroceram Sample 2.

Again each run was observed to cause a spray of sparks, flying debris and smoke. In run three at higher intensity, there were more sparks and smoke produced. Run two shattered the sample 4.5 seconds into the 7.5 second irradiation period. The sample was then irradiated once more in the same hole 2 due to an error in translating the sample. For run three, the back side showed charring seven seconds into the eleven second irradiation period. The dark spot on the back side started out circular with a diameter of approximately 1 mm.

Run Number	Crater Diameter (mm)	Depth (mm)	Ring Diameter (mm)
1	3	2	6
2	3	2.5	6
3	1	unknown	6

Table V.F.2.2 . Crater dimensions for Pyroceram Sample 2.

The irradiations did not produce a noticeable lip around the crater. However, upon completion of the irradiation, there was the presence of molten pyroceramic material in each crater which cooled into the black glossy material seen in Fig. (V.F.2.1). The crater dimensions are detailed in Table (V.F.1.2). The presence of the black glossy material prevented an accurate measurement of depths of the craters. The runs also produced a distinct circular ring around each crater probably produced by a temperature change in the sample around the crater. The char spot on the back side of the sample started out circular with a diameter of approximately 1 mm and ended up being elliptically shaped with the semi-major axis measuring 9mm and the semi-minor axis measuring 7 mm. None of the irradiations burned through sample 2. Figure (V.F.2.2)

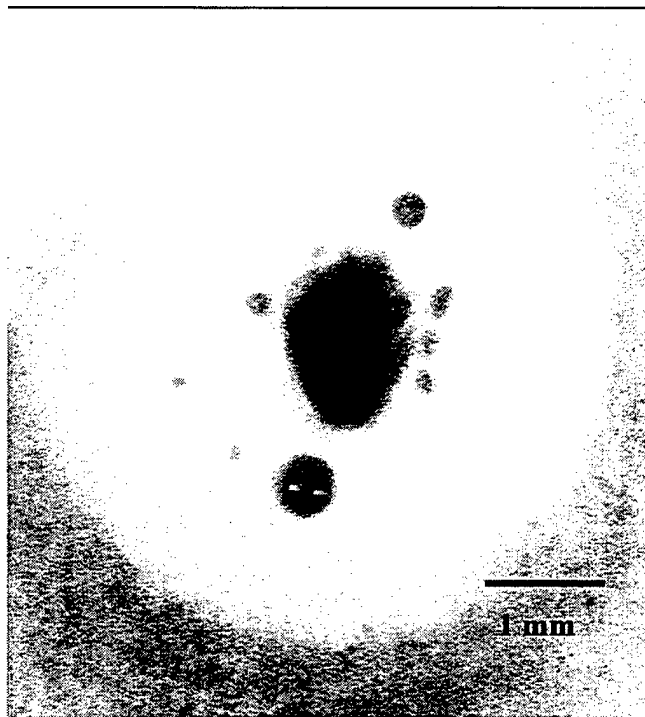


Figure V.F.2.2. Pyroceram Sample 2, run #3.

Sample 2, resulting from run three. The higher intensity beam produced a smaller spot size and thus a smaller crater. The presence of the black glossy material inhibits our ability to measure the depth of the crater, however, the charring on the back side of the sample suggests that the crater is quite deep.

VI. CONCLUSIONS

The Navy has a need for new ship-defense weapons. Computer simulations showed that CIWS is insufficient against state-of-the-art anti-ship missiles. Current Navy gun fire control systems aren't even configured to shoot down supersonic targets. With research and development, the Navy's Standard Missile will build on its current capability to shoot down ASMs. With the technology of ASMs on the rise, the Navy's Directed Energy Office is currently funding TJNAF to research and develop the FEL as a possible ship-defense weapon. The FEL is the best laser option for ship self-defense due to its unique characteristics.

This thesis studied the laser damage produced by the Free Electron Laser. Target materials were irradiated and observed. Each material's properties determine the kind and amount of damage caused by the laser. An in-depth study of a material's ability to withstand damage is critical in the development of future ship-defense directed energy weapons.

It is recommended that experiments be conducted with one irradiation per sample to eliminate the possibility of accumulating stress causing shattering. At a minimum, irradiations should be spaced out to cut down on possible interactions due to stress. In addition, manufacturers can be contacted to acquire experimental samples that are more uniform and suitable for experimentation. Other materials can be irradiated and studied in order to enlarge the database of information. TJNAF is currently planning experiments with wind to analyze the effects on laser induced damage. The TJNAF FEL will increase its power output in the near future and further experiments should be conducted at larger

power densities and spot sizes to determine effectiveness. The experiments in this thesis begin to develop scaling rules that can be used to predict damage from a larger scale ship-defense weapon without the extra cost.

The FEL's unique characteristics can be exploited to maximize possible damage to materials. The effects of the FELs short, powerful pulses should be studied in depth because it could reduce the power required by a directed energy weapon to induce damage.

LIST OF REFERENCES

- [1] Colson, W.B., Physics 4911 Course Notes, Naval Postgraduate School, 1998.
- [2] Cook, J.R. and Albertine, J.R., "High Energy Laser Weapon System," *Surface Warfare*, September/October 1997, Vol. 22, No. 5.
- [3] Davis, R., "Lasers will change the face of warfare," *USA Today*, 1 September 98.
- [4] Corrigan, T.J., "A Focus on the Navy's High Laser Program," Engineering Duty Officer Qualification Paper, U.S. Navy.
- [5] Herbert, P.A., "Anti-Ship Missile Defense and the Free Electron Laser," Master's Thesis, Naval Postgraduate School, December 1998.
- [6] Lyon, R.A., "Prime Power For Shipboard High-Average Power FELs," Master's Thesis, Naval Postgraduate School, December 1994.
- [7] Dylla, F., "FEL Commissioning Project Overview," brief presented at FEL Close Out Meeting held at TJNAF, Newport News, VA, April 26-27, 1999.
- [8] Cooper, A.W., and Crittenden, E.C., Physics 4254 Class Notes, Naval Postgraduate School, 1999.
- [9] Cooper, A.W., and Crittenden, E.C., Physics 4254 Class Notes, Naval Postgraduate School, 1999.
- [10] Rudie, N.J., *Principles and Techniques of Radiation Hardening*, Vol. XII, Western Periodicals Company, North Hollywood, 1986, pp 140-3.
- [11] Cook, J.R. and Albertine, J.R., "The Navy's High Energy Laser Weapon System," SPIE, Vol. 2988, pp 264-271.
- [12] Colson, W.B., *Laser Handbook*, Vol. 6, Chapter 5, editors Colson, W.B., Pellegrini, C. and Renieri, A., North-Holland, 1990, pp 116-194.
- [13] Schriempf, J.T., *Response of Materials to Laser Radiation: A Short course*, Naval Research Laboratory, Washington, DC, July 1974.
- [14] Shinn, M., TJNAF, personal communication.

INITIAL DISTRIBUTION LIST

1. Defense Technical Information Center2
8725 John J. Kingman Rd., STE 0944
Ft. Belvoir, VA 22060-6218

2. Dudley Knox Library2
Naval Postgraduate School
441 Dyer Rd.
Monterey, CA 93943-5101

3. Engineering & Technology Curricular Office, Code 34.....1
Naval Postgraduate School
Monterey, CA 93943

4. Professor William B. Colson, Code PH/Cw4
Department of Physics
Naval Postgraduate School
Monterey, CA 93943-5117

5. Professor Robert L. Armstead, Code PH/Ar1
Department of Physics
Naval Postgraduate School
Monterey, CA 93943-5117

6. Lieutenant Lee R. Short, USN1
707 Seneca, #A5
Ventura, CA 93001

7. John Albertine1
109 Kingwood Rd.
Annapolis, MD 21401

8. Joung R. Cook1
Research Physicists, Code 6655
Naval Research Laboratory
4555 Overlook Drive, SE
Washington, DC 20375-5000

9. Michelle Shinn1
TJNAF
12000 Jefferson Avenue
Newport News, VA 23606

10. George Neil1
TJNAF
12000 Jefferson Avenue
Newport News, VA 23606